

## RESEARCH ARTICLE

10.1002/2016JD025108

## Special Section:

East Asian Study of  
Tropospheric Aerosols and  
Impact on Cloud and  
Precipitation

## Key Points:

- Modeled shortwave radiation at the surface over East Asia decreases by 20 W m<sup>-2</sup> due to the aerosol direct effect
- The aerosol direct effect causes modeled PM<sub>2.5</sub> concentrations over East Asia to increase and ozone amounts to decrease
- PM<sub>2.5</sub> air quality benefits in East Asia associated with reducing absorbing aerosols may be partially offset by increases in ozone

## Supporting Information:

- Supporting Information S1

## Correspondence to:

J. Wang,  
jwang081@umd.edu

## Citation:

Wang, J., D. J. Allen, K. E. Pickering, Z. Li, and H. He (2016), Impact of aerosol direct effect on East Asian air quality during the EAST-AIRE campaign, *J. Geophys. Res. Atmos.*, 121, 6534–6554, doi:10.1002/2016JD025108.

Received 22 MAR 2016

Accepted 10 MAY 2016

Accepted article online 13 MAY 2016

Published online 2 JUN 2016

## Impact of aerosol direct effect on East Asian air quality during the EAST-AIRE campaign

Jing Wang<sup>1</sup>, Dale J. Allen<sup>1</sup>, Kenneth E. Pickering<sup>2</sup>, Zhanqing Li<sup>1,3,4</sup>, and Hao He<sup>1</sup>

<sup>1</sup>Department of Atmospheric and Oceanic Science, University of Maryland, College Park, Maryland, USA, <sup>2</sup>Atmospheric Chemistry and Dynamics Laboratory, NASA Goddard Space Flight Center, Greenbelt, Maryland, USA, <sup>3</sup>Earth System Science Interdisciplinary Center, University of Maryland, College Park, Maryland, USA, <sup>4</sup>State Key Laboratory of Earth Surface Processes and Resource Ecology, GCESS, Beijing Normal University, Beijing, China

**Abstract** WRF-Chem simulations were performed for the March 2005 East Asian Studies of Tropospheric Aerosols: an International Regional Experiment (EAST-AIRE) Intensive Observation Campaign (IOC) to investigate the direct effects of aerosols on surface radiation and air quality. Domain-wide, WRF-Chem showed a decrease of 20 W/m<sup>2</sup> in surface shortwave (SW) radiation due to the aerosol direct effect (ADE), consistent with observational studies. The ADE caused 24 h surface PM<sub>2.5</sub> (particulate matter with diameter < 2.5 μm) concentrations to increase in eastern China (4.4%), southern China (10%), western China (2.3%), and the Sichuan Basin (9.6%), due to different aerosol compositions in these four regions. Conversely, surface 1 h maximum ozone was reduced by 2.3% domain-wide and up to 12% in eastern China because less radiation reached the surface. We also investigated the impact of reducing SO<sub>2</sub> and black carbon (BC) emissions by 80% on aerosol amounts via two sensitivity simulations. Reducing SO<sub>2</sub> decreased surface PM<sub>2.5</sub> concentrations in the Sichuan Basin and southern China by 5.4% and decreased ozone by up to 6 ppbv in the Sichuan Basin and Southern China. Reducing BC emissions decreased PM<sub>2.5</sub> by 3% in eastern China and the Sichuan Basin but increased surface ozone by up to 3.6 ppbv in eastern China and the Sichuan Basin. This study indicates that the benefits of reducing PM<sub>2.5</sub> associated with reducing absorbing aerosols may be partially offset by increases in ozone at least for a scenario when NO<sub>x</sub> and VOC emissions are unchanged.

## 1. Introduction

Due to its large population and fast economic development, China is the largest emission source of aerosols and their precursors [Li *et al.*, 2011]. The observational study by Xin *et al.* [2007] showed an annual mean aerosol optical depth (AOD) of 0.43 at 19 stations in the Chinese Sun Hazemeter Network (CSHNET). These values are considerably higher than the global mean of AOD (0.19) over land from Moderate Resolution Imaging Spectroradiometer (MODIS) [Remer *et al.*, 2008]. Positive trends of AOD over the most populated regions in China (eastern and southern China) are observed from Sea-viewing Wide Field-of-view Sensor retrievals between 1997 and 2010 [Hsu *et al.*, 2012], indicating a degradation of air quality due to particulate matter (PM). In January 2013, an extremely severe and persistent haze spread over a large area of northern and eastern China with monthly average surface PM<sub>2.5</sub> (particulate matter with diameter < 2.5 μm) concentrations exceeding 225 μg/m<sup>3</sup> [K. Huang *et al.*, 2014] and daily surface PM<sub>2.5</sub> concentrations exceeding 500 μg/m<sup>3</sup> at several observation sites in Beijing and Shijiazhuang (the capital city of Hebei Province) [L. T. Wang *et al.*, 2014]. This record-breaking event has heightened concerns about PM pollution in China, which reduces visibility, threatens human health [Dockery *et al.*, 1993; Harrison and Yin, 2000], and has considerable impact on the radiative balance of the Earth, and consequently, the meteorological variables and chemical composition of the atmosphere through meteorology-chemistry-aerosol-radiation feedbacks [Intergovernmental Panel on Climate Change, 2014]. Ground-based measurements from 25 stations across China in 2005 have shown that the annual diurnal mean aerosol radiative forcing under clear skies is  $-15.7 \pm 8.9$  W/m<sup>2</sup> at the surface [Z. Li *et al.*, 2010].

Solar radiation is the major driver of tropospheric photochemistry through its impact on photolysis rates. Ozone among all the absorbing gases in the troposphere is the most sensitive to changes in shortwave radiation due to aerosols [Liu and Trainer, 1988; Thompson *et al.*, 1989; Madronich and Granier, 1992; Fuglestvedt *et al.*, 1994; Ma, 1995]. Therefore, the increasing aerosol loading in China [Hsu *et al.*, 2012] substantially influences concentrations of tropospheric ozone, a major air pollutant that is also harmful to human health. With the Sulfur Transport and Emissions Model (STEM), Tang *et al.* [2004] found that surface ozone concentrations

were reduced by 0.1% to 0.8% in northeastern China during the dust event of 4–14 April 2001 due to dust-induced changes in photolysis rates [Seinfeld and Pandis, 2006]. Tie *et al.* [2005] showed that with aerosols included in the radiation/photolysis scheme, surface layer photolysis rates of  $j(\text{O}_3)$  and  $j(\text{NO}_2)$  in eastern China were reduced, respectively, by 20 to 30% and 10 to 30% in winter as well as 5 to 20% and 1 to 10% in summer, leading to reductions in surface layer ozone concentrations of 2 to 4% in winter and minimal changes in summer. The formation rate of secondary aerosols, i.e., sulfate aerosol, is related to the abundance of the precursor gas ( $\text{SO}_2$ ) and atmospheric oxidants such as hydroxyl radical (OH), hydrogen peroxide ( $\text{H}_2\text{O}_2$ ), ozone ( $\text{O}_3$ ), methylhydroperoxide (MHP), and peroxyacetic acid (PAA) [Seinfeld and Pandis, 2006]. These atmospheric oxidants are formed via photochemical processes that are influenced by the ADE. The ADE-induced changes that affect the air quality not only include the changes in chemistry but also include the changes in meteorology. Forkel *et al.* [2012] studied the changes in ozone and PM triggered by the aerosol direct and indirect effects and found that mean surface ozone mixing ratios over continental Europe were increased by 10% mainly from the change in cloud cover due to both the semidirect effect and indirect effect.  $\text{PM}_{10}$  (particulate matter up to  $10\ \mu\text{m}$  in size) was decreased by  $2\text{--}5\ \mu\text{g m}^{-3}$  (20–50%) when only the direct effect and semidirect effect were included. Wang *et al.* [2015] investigated haze episodes in July 2008 over Jing-Jin-Ji and surrounding regions of China (Beijing, Tianjin, Hebei, East Shanxi, West Shandong, and North Henan) and showed that aerosol direct radiative forcing decreased the flux of solar radiation at the surface by more than 15% over most of the region leading to a 14% increase in surface  $\text{PM}_{2.5}$  due to ADE-related changes in meteorological conditions.

WRF-Chem [Grell *et al.*, 2005] is a version of the Weather Research and Forecasting (WRF) model that includes online interactions between meteorology, chemistry, and radiation. It can be used to relate the emissions of aerosols and their precursors to aerosol formation, growth, and transport and ultimately to study their impact on air quality, radiative balance, and the regional climate. Fast *et al.* [2006] simulated trace gases, PM, and aerosol direct radiative forcing in the Houston area over a 5 day summer period and found that the simulated surface shortwave radiation was closer to observations with the high bias reduced by up to 50% when the ADE was included in the shortwave radiative transfer scheme.

The 2005 East Asian Studies of Tropospheric Aerosols: an International Regional Experiment (EAST-AIRE) campaign was conducted in China to study the properties of aerosols and their precursors and gain insights into the aerosol direct and indirect effects on radiation, clouds, precipitation, atmospheric circulation, and the environment [Z. Li *et al.*, 2007]. An Intensive Observation Campaign (IOC) for EAST-AIRE was conducted near the Beijing metropolitan area in March 2005. High loadings of carbon monoxide (CO), sulfur dioxide ( $\text{SO}_2$ ),  $\text{NO}_y$ , and aerosols were observed during the campaign with large fluctuations due to synoptic processes [C. Li *et al.*, 2007]. Xia *et al.* [2007] calculated the aerosol direct radiative forcing on surface shortwave radiation at Xianghe observatory using an empirical equation to relate observed AOD to surface shortwave radiation and found an annual diurnal mean of  $-32.8\ \text{W/m}^2$  in 2005.

In this study, we conduct online-coupled WRF-Chem simulations from 1 to 31 March 2005, covering the EAST-AIRE IOC period. We begin the simulations on 22 February to minimize the impact of initial conditions on the results. Section 2.1 introduces the model setup and the sensitivity experiment design. The details of the observational data sets are described in section 2.2. In section 3.1, we evaluate the model-simulated meteorological variables, trace gases, and aerosol loading with observations. In section 3.2 the effects of ADE on radiation and air pollution for both ozone and particulate matter are demonstrated. Processes that control the distribution of ozone and  $\text{PM}_{2.5}$  (including major components) are investigated. Given the fact that China has implemented many regulations restricting pollutant emissions in order to lower  $\text{PM}_{2.5}$  levels, we performed WRF-Chem experiments to demonstrate the potential impact of ongoing emission reductions in section 3.3.

## 2. Model and Observational Data

### 2.1. WRF-Chem Model Setup

The model domain covers most of East Asia (Figure 1) with a horizontal resolution of 36 km and 32 vertical layers from the surface to 100 hPa with 14 layers in the lowest 2 km. Initial conditions, boundary conditions, and time-dependent sea surface temperatures (SSTs) were obtained from Global Forecast System (GFS) output archived on the National Center for Atmospheric Research (NCAR) Computational Information

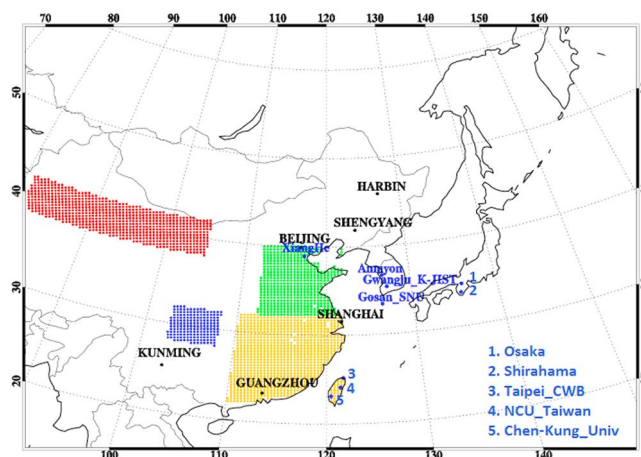


**Figure 1.** Domain of WRF-Chem simulation and analysis (within rectangle, 179 36 km grid cells from west to east and 149 36 km grid cells from south to north). Shaded regions: Western China (red, 38°N–42°N, 81°E–105°E), Sichuan Basin (blue, 26°N–34°N, 97°E–108°E), Southern China (yellow, 22°N–32°N, 110°E–122°E), and Eastern China (green, 32°N–40°N, 112°E–122°E). WRDC stations are in black and AERONET stations in blue.

Systems Laboratory (CISL) Research Data Archive (<http://rda.ucar.edu/datasets/ds083.2/>). Analysis nudging is not applied in order to allow for feedbacks between aerosols, radiation, and meteorology. The Model for Ozone and Related chemical Tracers (MOZART) [Emmons *et al.*, 2010] provided the initial and boundary conditions for trace gases and aerosols (<http://www.acd.ucar.edu/wrf-chem/mozart.shtml>).

We use WRF-Chem version 3.3 with the physics options listed in Table 1. The major chemical mechanisms used are the Carbon Bond Mechanism-Z (CBM-Z) photochemical mechanism [Zaveri and Peters, 1999], which contains 55 prognostic species and 134 reactions, with the lumped structure approach for organic species, and the Model for Simulating Aerosol Interactions and

Chemistry (MOSAIC) that uses a sectional approach, which divides the aerosol size distribution into eight discrete size bins defined by their lower and upper dry particle diameters. Aerosols in each bin are assumed to be internally mixed. Aerosol types included in MOSAIC are sulfate, nitrate, ammonium, chloride, sodium, other (unspecified) inorganics, organic carbon (OC), and black carbon (BC). Coagulation, nucleation, and secondary organic aerosol (SOA) formation processes are not included in MOSAIC in this version of WRF-Chem. The Fast-J photolysis scheme is modified to include the effect of prognostic aerosols and applied to calculate photolysis rates of chemical species (see Appendix A for details).

The anthropogenic emission inventory used in this work was developed by Zhang *et al.* [2009] for the years 2004–2005 with a horizontal resolution of 0.5° × 0.5°. It was prepared for the Intercontinental Chemical Transport Experiment-Phase B (INTEX-B) in 2006 [Singh *et al.*, 2009] and includes emissions for eight major species: SO<sub>2</sub>, NO<sub>x</sub>, CO, PM<sub>10</sub>, PM<sub>2.5</sub>, BC, OC, and nonmethane volatile organic compounds (NMVOC). The emissions for inorganic species are divided into four sectors: industry, transportation, power plant, and residential. Emissions for anthropogenic NMVOC species are speciated based on the RADM2 chemical mechanism and grouped in categories of biofuel burning, fossil fuel burning, industry, transportation, and power plant. Since NH<sub>3</sub> emissions are not available from the INTEX-B emission inventory, data with 0.25° × 0.25° horizontal resolution from Model Inter-Comparison Study for Asia (MICS) 2008 emission inventory are used [Huang *et al.*, 2012]. Biomass burning emissions of CO, NO<sub>x</sub>, other carbon compounds, and particulate matter are obtained from the Global Fire Emissions Database (GFED) Version 3.1 with a spatial resolution of 0.5° × 0.5° degrees and a temporal resolution of 1 day [van der Werf *et al.*, 2010; Mu *et al.*, 2010]. Biogenic VOC (BVOC) emissions account for ~90% of global VOC emissions [Guenther *et al.*, 1995]. BVOC emissions are important during March in the southern

**Table 1.** Configuration of WRF-Chem (V3.3) Model

	Model
Longwave radiation	Rapid Radiative Transfer Model (RRTM) [Mlawer <i>et al.</i> , 1997]
Shortwave radiation	Goddard [Chou and Suarez, 1994]
Land surface	NOAH [Chen and Dudhia, 2001]
Surface layer	Quasi-normal Scale Elimination (QNSE) [Sukoriansky <i>et al.</i> , 2005]
Boundary layer	QNSE [Sukoriansky <i>et al.</i> , 2005]
Cumulus clouds	Grell 3D [Grell and Devenyi, 2002]
Cloud microphysics	Morrison [Morrison <i>et al.</i> , 2009]
Gas phase chemistry	CBM-Z [Zaveri and Peters, 1999]
Aerosol module	MOSAIC eight bins [Zaveri <i>et al.</i> , 2008]
Photolysis	Fast-J [Barnard <i>et al.</i> , 2004; Wild <i>et al.</i> , 2000]

**Table 2.** Experiment Setup

	Description
Base	Include both aerosol direct and indirect effects
Base_No_ADE	Include only aerosol indirect effect
SO <sub>2</sub> × 0.2	Same setting as Base with SO <sub>2</sub> emission reduced to 20% of INTEX-B values
BC × 0.2	Same setting as Base with BC emission reduced to 20% of INTEX-B values

portion of our modeling domain. We simulated these emissions using v2.04 of the Model of Emissions of Gases and Aerosols from Nature (MEGAN) [Guenther *et al.*, 2006] that is a standard component of v3.3 WRF-Chem. MEGAN v2.4 is driven by land cover information from NCAR (<http://www.acom.ucar.edu/wrf-chem/download.shtml>) and meteorological variables from the prognostic WRF-Chem simulation.

Two WRF-Chem experiments (Table 2) were conducted to investigate the effects of the ADE: (1) All aerosol effects are included (Base) and (2) aerosol direct effect is removed (Base\_No\_ADE). We evaluate the meteorological conditions, trace gas concentrations, and aerosol properties simulated from the Base case with observations. The total aerosol radiative forcing can be decomposed into three components: direct radiative forcing, cloud radiative forcing, and surface albedo forcing [Ghan, 2013]. In this study, the first term was determined by subtracting the results from the Base\_No\_Ade simulation that did not pass aerosols to the Goddard shortwave radiation scheme from the Base simulation that passed prognostic aerosols to the shortwave scheme. The Goddard shortwave radiation scheme as configured for WRF-Chem V3.3 uses simulated aerosol and cloud optical information, fixed CO<sub>2</sub> (300 ppm), and prescribed ozone profiles. Interactions between prognostic aerosol and photolysis rates are included in the Fast-J module in the BASE case (see Appendix A). However, no aerosols are passed to the Fast-J module in the Base\_No\_ADE case.

Because air quality is currently poor in much of China, we perform two additional sensitivity simulations to test the potential impact of pollutant emission regulations. Since sulfate and BC are different types of aerosols in terms of optical properties, i.e., scattering and absorbing, reducing the emissions of sulfate precursor (SO<sub>2</sub>) and BC should have different effects. Therefore, we carried out two sensitivity simulations: (a) SO<sub>2</sub> emissions reduced to 20% of INTEX-B emissions (SO<sub>2</sub> × 0.2), chosen based on the fractional change between 2050 and 2005 SO<sub>2</sub> emissions from the Intergovernmental Panel on Climate Change Representative Concentration Pathways (RCP) 4.5 scenario (<http://tntcat.iiasa.ac.at:8787/RcpDb/dsd?Action=htmlpage&page=welcome#intro>), while emissions of other trace gases and PM are unchanged from INTEX-B; (b) BC emissions reduced to 20% of INTEX-B emissions (BC × 0.2), while emissions of other trace gases and PM are unchanged from INTEX-B. An 80% reduction of BC reduces Chinese BC emissions to approximately current U.S. BC emissions (see section 3.3). The difference between the reduced emission simulations and the Base simulation shows the impact of reducing pollutant emissions on radiation, meteorological variables, and air quality.

## 2.2. Observational Data

In situ observations of meteorological fields (ambient temperature, relative humidity, surface pressure, and wind speed), trace gas (O<sub>3</sub>, CO, SO<sub>2</sub>, NO, and NO<sub>y</sub>) concentrations, and aerosol optical properties were made at the Xianghe Atmospheric Observatory (39.798°N, 116.958°E; 35 m above sea level) during the EAST-AIRE IOC period [C. Li *et al.*, 2007]. This observation site sits between two megacities, southeast of Beijing and northwest of Tianjin (a megacity with population about 12.9 million), surrounded by agricultural land, densely occupied residential areas, and light industry. Therefore, there were frequent pollution plumes passing over the site with either urban or rural origins [C. Li *et al.*, 2007].

Daily ground observations of the surface temperature from 743 stations across China [Li and Yan, 2009] were used to evaluate the WRF-Chem simulation of surface temperature and to investigate the impact of aerosol on the surface temperature.

The Moderate Resolution Imaging Spectroradiometer (MODIS) instruments aboard NASA's Terra and Aqua satellites, with overpass times at 10:30 A.M. and 1:30 P.M. local time, respectively, are making near-global daily observations of the Earth in a wide spectral range (0.41–15 μm) [Remer *et al.*, 2005]. Spectral AOD and aerosol size parameters can be derived from these measurements. Level 2 MODIS Terra and Aqua data with 10 km spatial resolution (collection 5, deep blue retrieval algorithm) at the locations of AERONET [Holben *et al.*, 1998] stations obtained from Geospatial Interactive Online Visualization ANd aNalysis Infrastructure (GIOVANNI) (<http://giovanni.gsfc.nasa.gov/aerostat/>) over the study region are used to evaluate the model simulation of AOD.

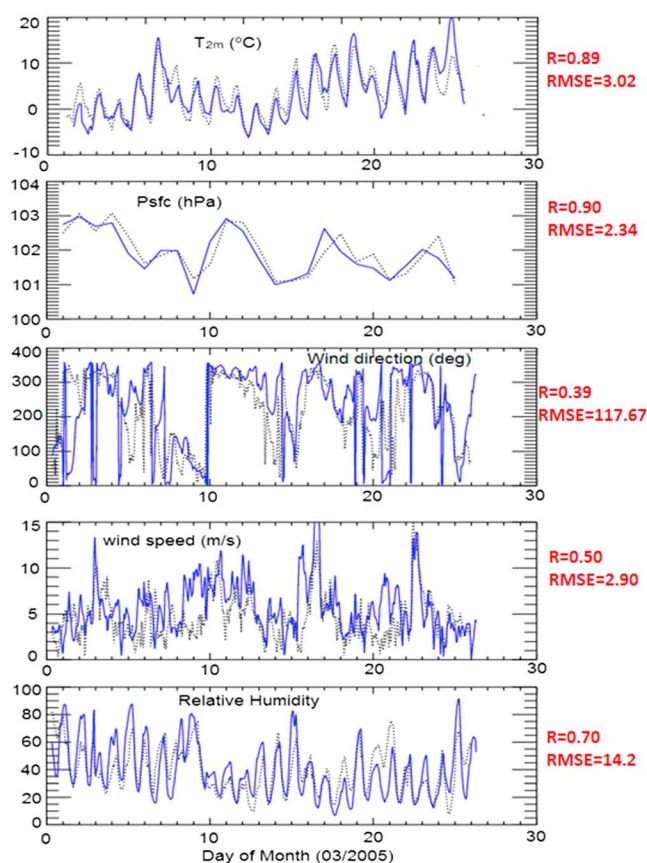


**Figure 2.** Comparison of meteorological variables: hourly surface temperature at 2 m, daily average surface pressure, hourly surface wind speed, and hourly relative humidity from WRF-Chem simulation versus hourly averaged observations at Xianghe Observatory in March 2005 (black dots: observation; blue lines: model).

in China [Li and Yan, 2009]. The average temporal correlation of the hourly values is 0.82 with about 70% of stations exceeding 0.8. After the seasonal cycle is removed, the domain-wide average temporal correlation is still 0.75, indicating that the model captures the temporal evolution of surface temperature in most parts of China. The magnitudes for all the variables are reasonably reproduced, with biases less than 20%. We find that the simulated wind field is sensitive to the boundary layer physics, land use, and surface schemes used in the model. By changing the combination of land surface layer scheme and boundary layer scheme from the revised MM5 Monin-Obukhov scheme and Yonsei University (YSU) scheme [Hong *et al.*, 2006], which are used by Fast *et al.* [2006], to the Quasi-normal Scale Elimination (QNSE) land surface and boundary layer Scheme [Sukoriansky *et al.*, 2005], we reduced the high biases in wind speed from 40% to 20%. We compared the March total precipitation with data from the Global Precipitation Climatology Project. Figure S1 in the supporting information shows that the model does a reasonable job of reproducing the precipitation distribution with a spatial correlation of 0.66. However, the model does overestimate the precipitation in the whole domain with an average bias of 28%, although low biases ( $\sim -13\%$ ) were found in the southeast China.

Hourly averaged trace gas measurements at Xianghe Observatory from the EAST-AIRE campaign were used to evaluate the performance of WRF-Chem (Figure 3). Temporal fluctuations of CO and SO<sub>2</sub> are moderately correlated with observations with substantial underestimation on highly polluted days. The underestimation of peaks is expected due to the relatively coarse resolution of both the emission inventory and the WRF-Chem simulation.

Figure 4 shows the correlation between pollutant levels and wind speed and direction. The most frequent wind directions (Figure 4a) at Xianghe simulated by WRF-Chem are from the northwest quadrant (where Beijing is located), which is consistent with the observations. However, the model produces more strong

Tropospheric NO<sub>2</sub> columns from Ozone Monitoring Instrument (OMI) are obtained from version 2 of the “Derivation of OMI tropospheric NO<sub>2</sub>” project (DOMINO) [Boersma *et al.*, 2011]. The OMI instrument has a 13 × 24 km spatial resolution at nadir and produces global coverage over cloud-free locations in one day [Levelt *et al.*, 2006].

### 3. Results and Discussion

#### 3.1. Model Evaluation Against Observations

The meteorological fields from the Base case simulation agree well with surface temperature, pressure, wind fields, and relative humidity observations at Xianghe Observatory (Figure 2). The temporal variations of modeled surface temperature, pressure, and RH are well correlated with observations (correlation coefficient  $R=0.7-0.9$ ), and the wind speed is moderately correlated ( $R=0.5$ ) with observations, indicating that WRF-Chem can capture the evolution of synoptic systems passing Xianghe Observatory. The monthly average 2 m temperature simulated from Base case (Figure 9c) agrees well with observations (not shown in the figure) from 743 meteorological stations

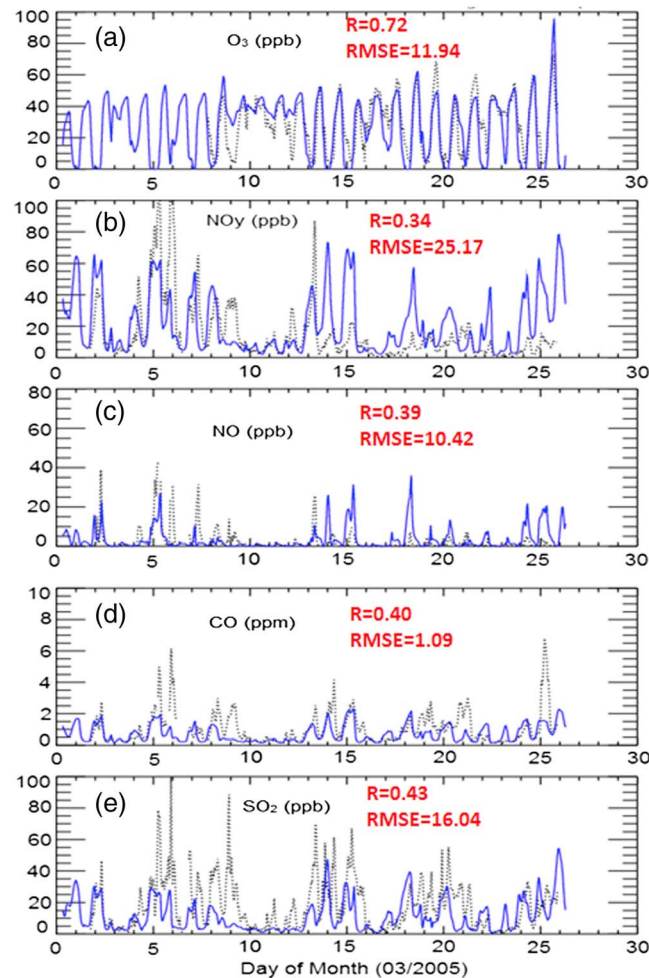


**Figure 3.** Comparison of hourly average trace gases: (a)  $O_3$ , (b)  $NO_y$ , (c) NO, (d) CO, and (e)  $SO_2$  from WRF-Chem simulation and observations at Xianghe Observatory from 2 to 26 March (black dots: observation; blue lines: model).

winds from the north and northeast than observations. A portion of the low biases is caused by the 20% overestimation of wind speeds and hence dilution during periods of stagnation. Based on the observed and modeled wind roses (Figure 4a), the frequency of easterly winds is underestimated by WRF-Chem. Consistently, most of the high CO mixing ratios (larger than 3 ppm) observed at Xianghe (Figure 4b) occur when winds come from the east. Therefore, an underpredicted frequency of easterly winds in the model is another reason for the low bias of CO concentration at Xianghe. However, model CO amounts are low regardless of wind direction, indicating that there is likely a low bias in the CO emissions. The model captures the diel cycles of ozone and NO.  $O_3$  is well simulated starting on 12 March, while from 9 to 12 March, WRF-Chem overestimates the nighttime ozone. This high bias in nighttime ozone is related to the underestimation of NO during these days, which slows down the ozone titration process. WRF-Chem underestimates NO levels for 6 to 12 March, which is consistent with the low bias of CO and  $SO_2$  during these days, after cold frontal passages on 6 and 9 March [C. Li *et al.*, 2007]. After the cold fronts, the wind speed is significantly overestimated, with biases approaching twice the monthly average bias.

Model output is compared to retrieved OMI tropospheric  $NO_2$  columns for March 2005 in Figure 5. The domain-wide spatial correlation between WRF-Chem and the DOMINO tropospheric  $NO_2$  column is 0.85 with a mean bias of about 16%, demonstrating that the model can reproduce the spatial pattern and magnitude of tropospheric  $NO_2$  column amounts with a small high bias. The high bias is mainly found in the Sichuan basin (southwest China) and eastern China. Zhao and Wang [2009] estimated  $NO_x$  emissions from fossil fuel combustion in East Asia constrained by assimilated inversion of daily OMI tropospheric  $NO_2$  columns in a Regional chEmical trAnsport Model. They found that the a posteriori  $NO_x$  emissions from the assimilated inversion are 13% lower than the a priori  $NO_x$  emissions (INTEX-B), which indicates that the  $NO_x$  emissions used in our work are biased high and likely explain a portion of the high biases in simulated NO and  $NO_2$ .

The evaluation of simulated aerosol properties is shown in Figure 6. WRF-Chem is able to reproduce the buildup and decrease of aerosols (Figure 6a); however, WRF-Chem tends to underpredict AOD on highly polluted days as indicated by observations. Comparing the aerosol scattering coefficient (Figure 6c) and absorption coefficient (Figure 6b), we found that the absorption coefficient shows better agreement with observations (although the model underestimates the peak values) than the scattering coefficient, indicating that the underestimation of AOD is mainly contributed by the underestimated aerosol scattering coefficient. A test run with  $5 \times SO_2$  emissions enhances scattering coefficients at Xianghe by less than 10%, which indicates that the underestimated scattering coefficients are not caused by a low bias in emissions of the sulfate precursor. The low relative humidity in this region during March leads to the low sensitivity of the scattering

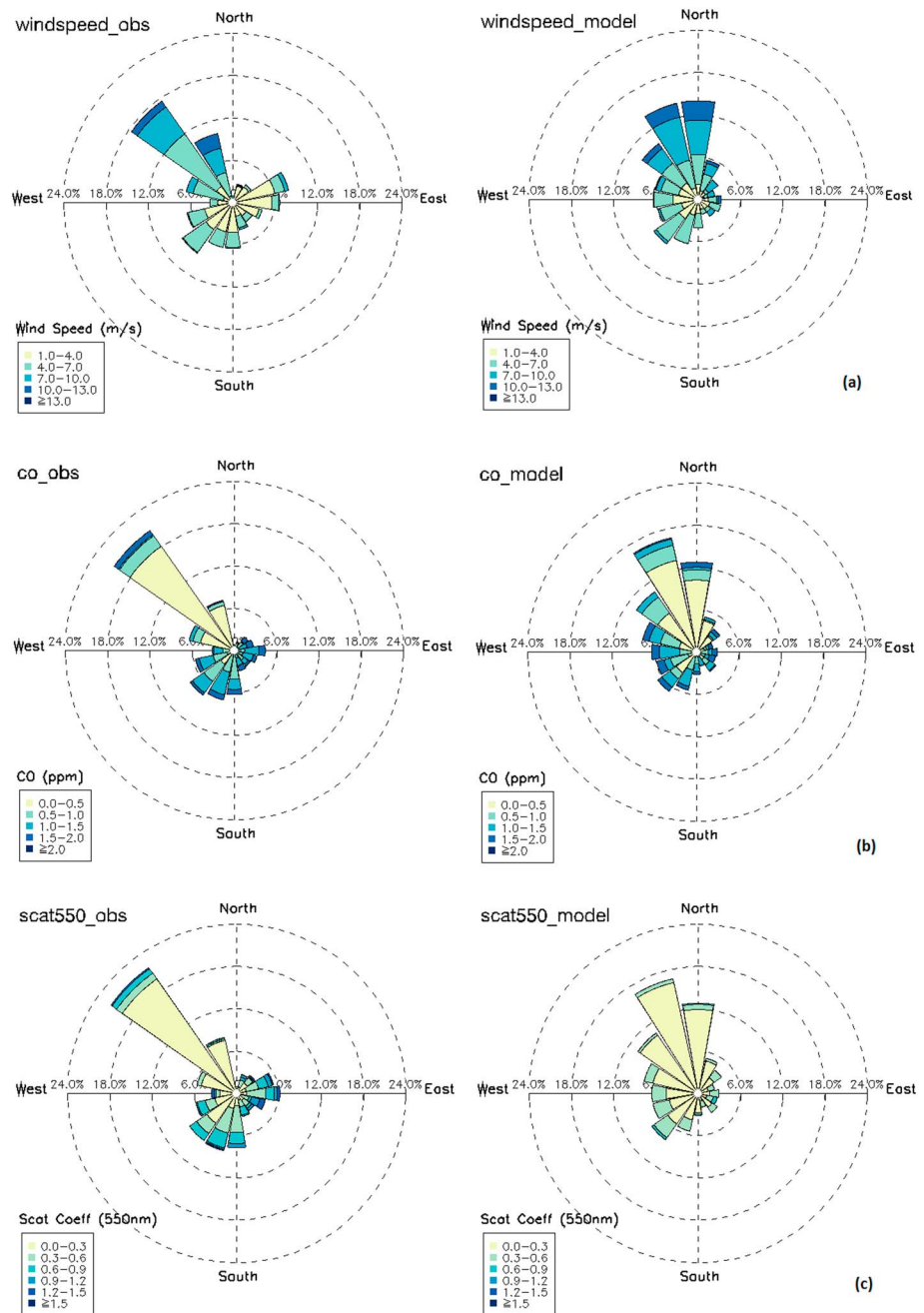


**Figure 4.** Comparisons of (a) wind roses, (b) CO roses, and (c) scattering coefficient roses at Xianghe Observatory from observations (left column) and WRF-Chem (right column). The length of each wedge shows the frequency that the wind comes from one of the 16 directions. The colored sections of each wedge show the frequency, the wind speed, CO mixing ratio, and scatter coefficient take on values shown in the legend.

coefficient to the emissions of the sulfate precursor since the formation of sulfate via aqueous chemistry is suppressed. We conduct the scattering coefficient rose analysis, similar to CO (Figure 4), and find that WRF-Chem underestimates scattering coefficients in all directions, suggesting that the potential sources of the bias not only include the bias in wind field but also include the large uncertainty of the anthropogenic OC emissions ( $\pm 258\%$ ) from INTEX-B emission inventory [Zhang *et al.*, 2009].

The lack of secondary organic aerosol (SOA) formation in WRF-Chem 3.3 may also contribute to the low bias in aerosol scattering coefficient, scattering coefficient, aerosol optical depth, and single-scattering albedo and affect the radiation budget [Fast *et al.*, 2006]. Jiang *et al.* [2012] studied seasonal and spatial variations in

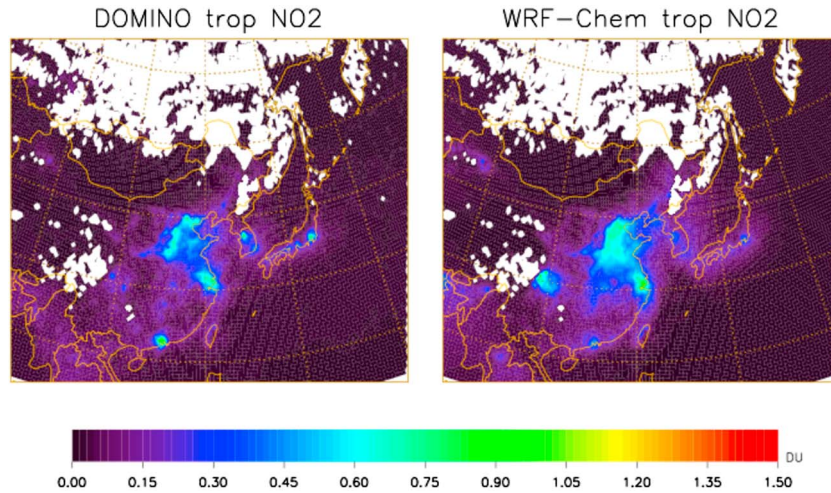


**Figure 5.** Monthly mean tropospheric NO<sub>2</sub> from (left) OMI DOMINO data and (right) WRF-Chem simulation AER\_all in March 2005. (Unit, Dobson unit, 1 DU = 2.69 × 10<sup>16</sup> molecules/cm<sup>2</sup>). The tropospheric NO<sub>2</sub> column is derived from DOMINO v2.0 retrieval algorithm [Boersma et al., 2011]. Level 2 data are used with the averaging kernel applied to the model.

SOA concentrations over China in 2006 using WRF-Chem coupled with the secondary organic aerosol model and an additional SOA module that accounts for SOA formation from isoprene. As in our work, their study used the INTEX-B emission inventory for anthropogenic VOC emissions and MEGAN model coupled with WRF-Chem for biogenic VOC emissions. Thus, our SOA concentrations would likely be similar to theirs if we used a version of WRF-Chem that included SOA formation. They found that the mean surface concentration of total SOA over China in spring was 0.94 μg/m<sup>3</sup>, which was 37% of the mean summertime SOA concentration. The mean concentration in early spring was even lower. Anthropogenic sources were responsible for 41% of the springtime SOA, while biogenic sources were responsible for 59% of the SOA. In our simulation, the mean PM<sub>2.5</sub> concentration over China was 46.3 μg/m<sup>3</sup> indicating that in a mean sense SOA comprised a small percent (2%) of total PM<sub>2.5</sub>.

However, recent observations indicate that SOA and anthropogenic SOA in particular play an important and “not yet widely recognized” role in urban wintertime haze events [K. Huang et al., 2014; R.-J. Huang et al., 2014] contributing 30% to 77% of total PM<sub>2.5</sub> in Beijing, Shanghai, Guangzhou, and Xi’an during severe haze events in January 2013. In summary, the lack of a SOA module in v3.3 of WRF-Chem is not a show stopper as SOA concentrations are usually relatively small during the early spring; however, it is a weakness that must be considered when interpreting results, especially during intense haze events.

In addition, we evaluate the WRF-Chem simulated AOD with AERONET measurements and MODIS Terra and Aqua at the locations of AERONET sites (Figure 7). The correlation between MODIS and AERONET observations is above 0.86 at these stations. The comparison shows that WRF-Chem captures the temporal variation moderately well with correlations

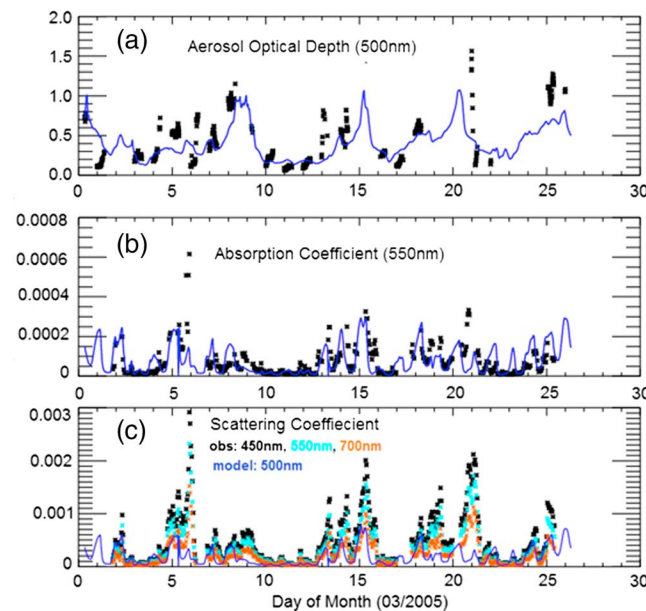


**Figure 6.** Comparison of aerosol properties: (a) AOD, (b) absorption coefficient at 550 nm, and (c) scattering coefficient from hourly WRF-Chem simulation outputs (dark blue lines) and observations (symbols) at Xianghe Observatory from 2 to 26 March. Observed absorption coefficient and scattering coefficient are hourly averaged from EAST-AIRE IOC data.

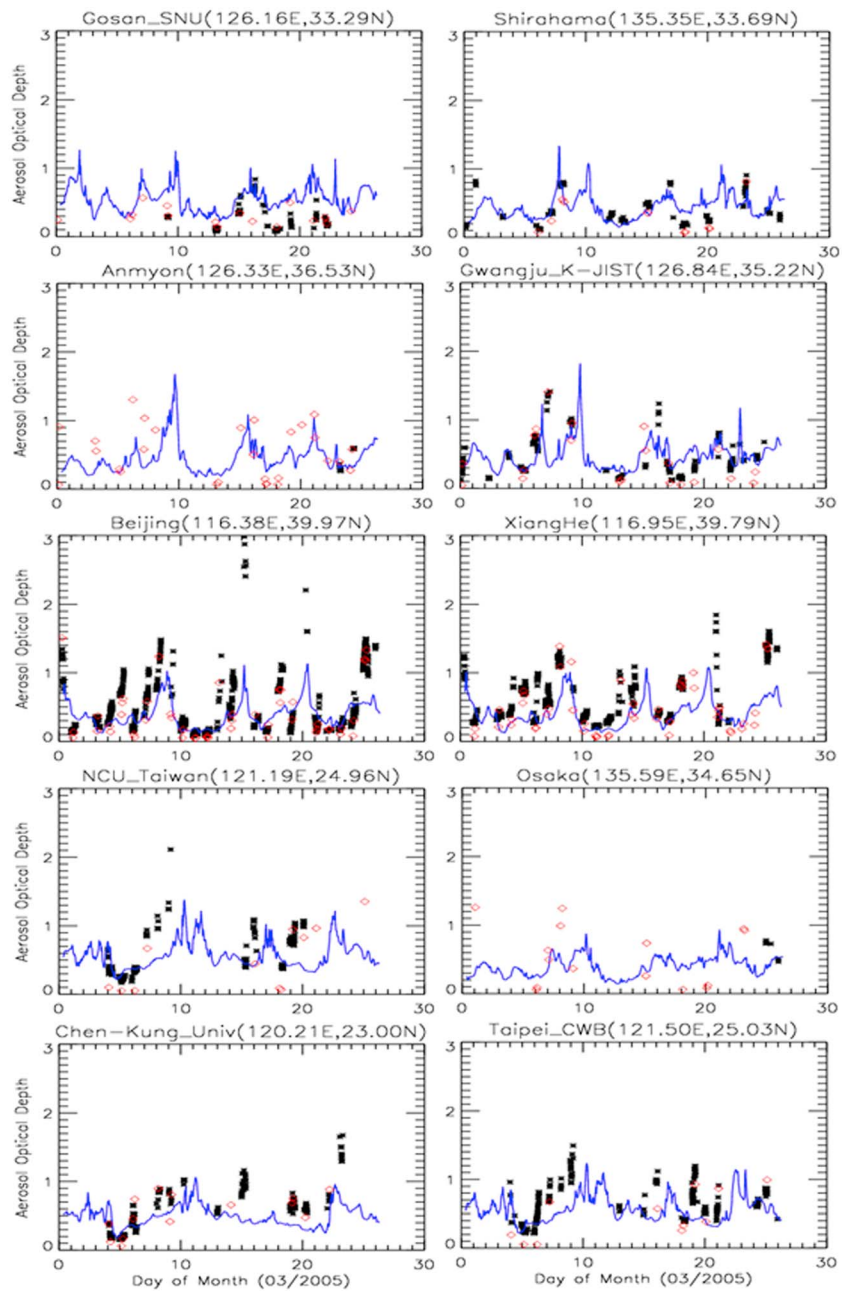


**Figure 7.** AOD values from AERONET (black asterisks), MODIS (red diamonds), and WRF-Chem simulation (blue lines) are compared at the location of 10 AERONET sites.

(AERONET and MODIS combined) higher than 0.5 at 8 out of 10 stations. WRF-Chem simulated AOD values are also close to AERONET and MODIS values, demonstrating the ability of WRF-Chem to simulate the aerosol loading. In general, the model slightly underestimates AOD with respect to AERONET (Table 3), with biases less than 30% at seven stations. Low biases are largest in urban areas on highly polluted days ( $AOD > 1$ ) suggesting that the model is unable to capture local peaks due to its coarse spatial resolution. On the other hand, WRF-Chem overestimates the aerosol loading at the coastal rural site Gosan\_SNU (Table 3).

### 3.2. Aerosol Direct Effect

As shown in section 3.1, WRF-Chem reproduces the observed meteorological fields with high temporal correlations ( $R > 0.7$ ) and low biases. The concentrations of trace gases are moderately well simulated

**Table 3.** Statistics of Aerosol Optical Depth From AERONET and WRF-Chem

Station	AERONET		Model		Bias	Correlation
	Mean	SD	Mean	SD		
Gosan_SNU	0.26	0.18	0.53	0.13	0.27	0.52
Shirahama	0.39	0.21	0.39	0.13	0.007	0.54
Anmyon	0.37	0.13	0.35	0.14	-0.02	0.60
Gwangju_K-JIST	0.47	0.32	0.45	0.18	-0.02	0.38
Beijing	0.52	0.49	0.36	0.19	-0.14	0.72
Xianghe	0.60	0.35	0.35	0.16	-0.25	0.72
NCU_Taiwan	0.62	0.37	0.43	0.11	-0.19	0.37
Osaka	0.65	0.15	0.47	0.06	-0.18	0.25
Chen-Kung_Univ	0.63	0.36	0.45	0.14	-0.18	0.57
Taipei_CWB	0.64	0.29	0.45	0.13	-0.19	0.38

( $0.4 < R < 0.7$ ) with  $\text{NO}$  and  $\text{NO}_y$  overestimated and  $\text{SO}_2$  and  $\text{CO}$  underestimated. Temporal fluctuations in AOD are also well ( $R > 0.7$ ) simulated although some peaks are underestimated at highly polluted locations and on highly polluted days. With the reasonable capability in simulating the interaction between meteorology, chemistry, and aerosol, we investigate the ADE by comparing the differences between sensitivity runs Base and Base\_No\_ADE.

The feedbacks of aerosols on surface shortwave radiation are examined in Figure 8, which compares model output with measurements from the World Radiation Data Center (WRDC) at six Chinese stations. The upper three stations in Figure 8 (Beijing, Shengyang, and Harbin) are from northern China, and the lower three stations (Kunming, Guangzhou, and Shanghai) are from southern China (Figure 1, black stations). The Base case captures the trend and magnitude of the surface radiation moderately well, with temporal correlations between 0.4 and 0.7, and an average bias of  $61.5 \text{ W/m}^2$  (Table 4). Biases are largest at all stations for the Base\_No\_ADE case that does not include ADE. The average aerosol direct forcing on surface radiation for these six stations is  $-21.2 \text{ W/m}^2$  and is  $-27 \text{ W/m}^2$  for Beijing station, which is close to the value obtained at Xianghe [Xia et al., 2007] by subtracting the calculated radiative flux assuming aerosol-free conditions from the observed surface radiation. Figure 8 also shows temporal variations of daily AOD at each station. Negative correlation coefficients between AOD and surface SW radiation ranging from  $-0.50$  to  $-0.82$  are found, suggesting the important impact of the ADE on surface SW radiation.

Figure 9a shows mean model surface shortwave radiation from the Base case for March 2005. The spatial pattern shows a gradual decrease of surface SW radiation from south to north primarily due to the change in Sun angle with latitude. A maximum is also seen over the elevated Tibetan plateau and relatively low values over the Sichuan Basin and southern China. Aerosols lead to the domain-wide decrease of surface

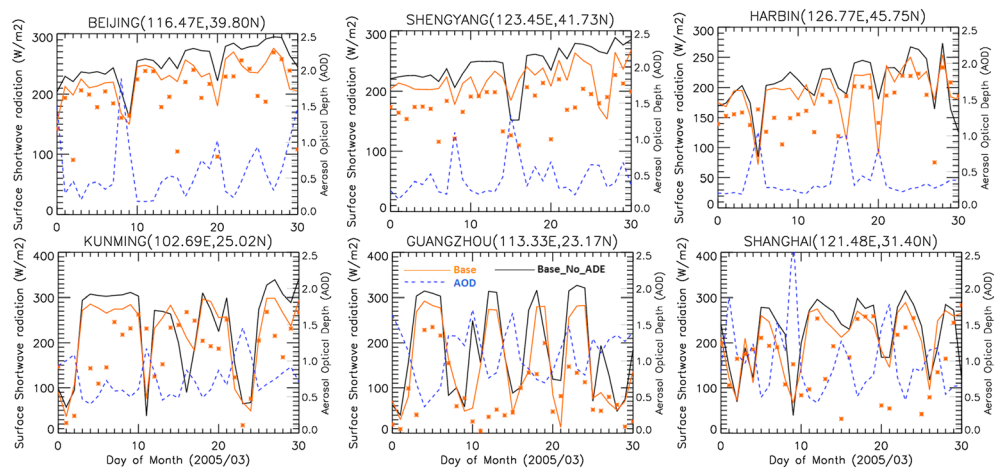


**Figure 8.** Daily surface shortwave radiation from World Radiation Data Center (red asterisks) and two WRF-Chem simulations (red: Base; black: Base\_No\_ADE) for March 2005. The blue dashed line is the simulated daily average AOD from Base run at each station.

**Table 4.** Statistics of the Comparison of Surface Shortwave Radiation Between WRF-Chem and WRDC Data

	Base			Base_No_ADE		
	Correlation	Bias ( $W/m^2$ )	RMSE <sup>a</sup>	Correlation	Bias ( $W/m^2$ )	RMSE
Beijing	0.69	82.6	44.6	0.63	109.7	66.7
Shengyang	0.50	45.2	52.3	0.78	69.3	70.4
Harbin	0.45	52.3	46.8	0.48	66.7	54.3
Kunming	0.44	73.8	103.2	0.35	87.9	123.2
Guangzhou	0.60	105.4	103.1	0.50	168.8	134.4
Shanghai	0.51	9.6	79.6	0.35	24.1	99.2

<sup>a</sup>RMSE, root-mean-square error.

SW radiation over land due to the ADE with an average of  $-20 W/m^2$  (Figure 9b). The reduction is higher than the domain average over the four regions of interest (Table 5): western China ( $-30.8 W/m^2$ ), eastern China ( $-27.1 W/m^2$ ), Sichuan Basin ( $-25.8 W/m^2$ ), and southern China ( $-22.8 W/m^2$ ), as  $PM_{2.5}$  concentrations are high with respect to the domain average in these regions (Figure 10a). The percentage changes of the surface SW radiation due to the ADE in these four regions range from  $-11.7\%$  to  $-14.3\%$ , which is comparable with the 15% decrease shown in Wang *et al.* [2015].

The comparison of the hourly surface SW radiation shows a good agreement between the observation at Xianghe and the WRF-Chem (Base) simulation (Figure 11, top) on two cloud-free days (12 and 13 March 2005). The mean bias is  $8 W/m^2$  for these two days, and the highest bias occurs at noon and is  $43 W/m^2$  (5% higher than the observation). The high bias in the model simulated surface radiation during these two clear-sky days comes from the underestimated AOD by WRF-Chem. The ADE on the surface SW radiation (Figure 11, bottom) at Xianghe is up to  $-40 W/m^2$  with a diurnal mean of  $-15.6 W/m^2$  for these two days.

Surface temperatures are generally reduced by the ADE (Figure 9d), with an average reduction of about  $-0.73^\circ C$  over land. The largest impacts on surface temperature in China are shown in the Sichuan Basin, cooling this region by about  $-1.4^\circ C$ . Changes of relative humidity (RH) differ between the four regions, with decreases in eastern China (3.3%), southern China (1.7%), and the Sichuan Basin (0.5%) and an increase in western China (1.8%).

The impacts of the ADE on surface concentrations of  $PM_{2.5}$  and its components are shown in Figure 10. Monthly mean surface  $PM_{2.5}$  is high over eastern China ( $116 \mu g/m^3$ ), southern China ( $76 \mu g/m^3$ ), Sichuan Basin ( $116 \mu g/m^3$ ), and western China ( $155 \mu g/m^3$ ) (see Figure 1 for latitude/longitude boundaries of each region). Dust is the dominant component in all regions, while sulfate is most important in the Sichuan Basin, and nitrate, BC, and OC all have high values over the Sichuan Basin and eastern China.  $PM_{2.5}$  in east China is composed of dust (61.6%), sulfate (7.1%), nitrate (9.4%), BC (4.8%), and OC (11.4%). In southern China, dust is 58.1%, sulfate is 10%, OC is 9.8%, nitrate is 10.8%, and BC is 3.3% of the total  $PM_{2.5}$ . Composition of  $PM_{2.5}$  in western China is mainly dust aerosols (97.4%). In the Sichuan Basin,  $PM_{2.5}$  components include 58.7% dust, 10.6% sulfate, 7.7% nitrate, 3.8% BC, and 12.8% OC.

The ADE has a different impact on  $PM_{2.5}$  components in different regions. The ADE increases the total  $PM_{2.5}$  concentration in all four regions (4.4% in eastern China, 10% in southern China, 2.3% in western China, and 9.6% in the Sichuan Basin) due to an increase in all the primary aerosols (dust, BC, and OC) (Table 6). The percentage increases in  $PM_{2.5}$  found here are less than 14% found by Wang *et al.* [2015], which is to be expected as they show an average over a hazy period in July while we show monthly averages. The enhancement of primary aerosols can be attributed to a thinner mean planetary boundary layer height (PBLH) and a more stabilized atmosphere. The PBLH is mainly driven by the strength of the thermal and mechanistic turbulence. Cooler surface temperatures cause weaker thermal turbulence; therefore, the PBLH gets thinner (Figure 9h), with the regional average decrease ranging from 75 m to 138 m (Table 5), therefore concentrating pollutants. The ADE also tends to stabilize the atmosphere. We use the temperature lapse rate between the surface and 700 hPa (Figure 9i) as a proxy for atmospheric stability as applied in Storer *et al.* [2014]. The temperature lapse rate reduces domain wide (Table 5), which means that the temperature difference between the surface and 700 hPa is smaller, and air parcels have less tendency to move upward, therefore constraining the vertical mixing of aerosols.

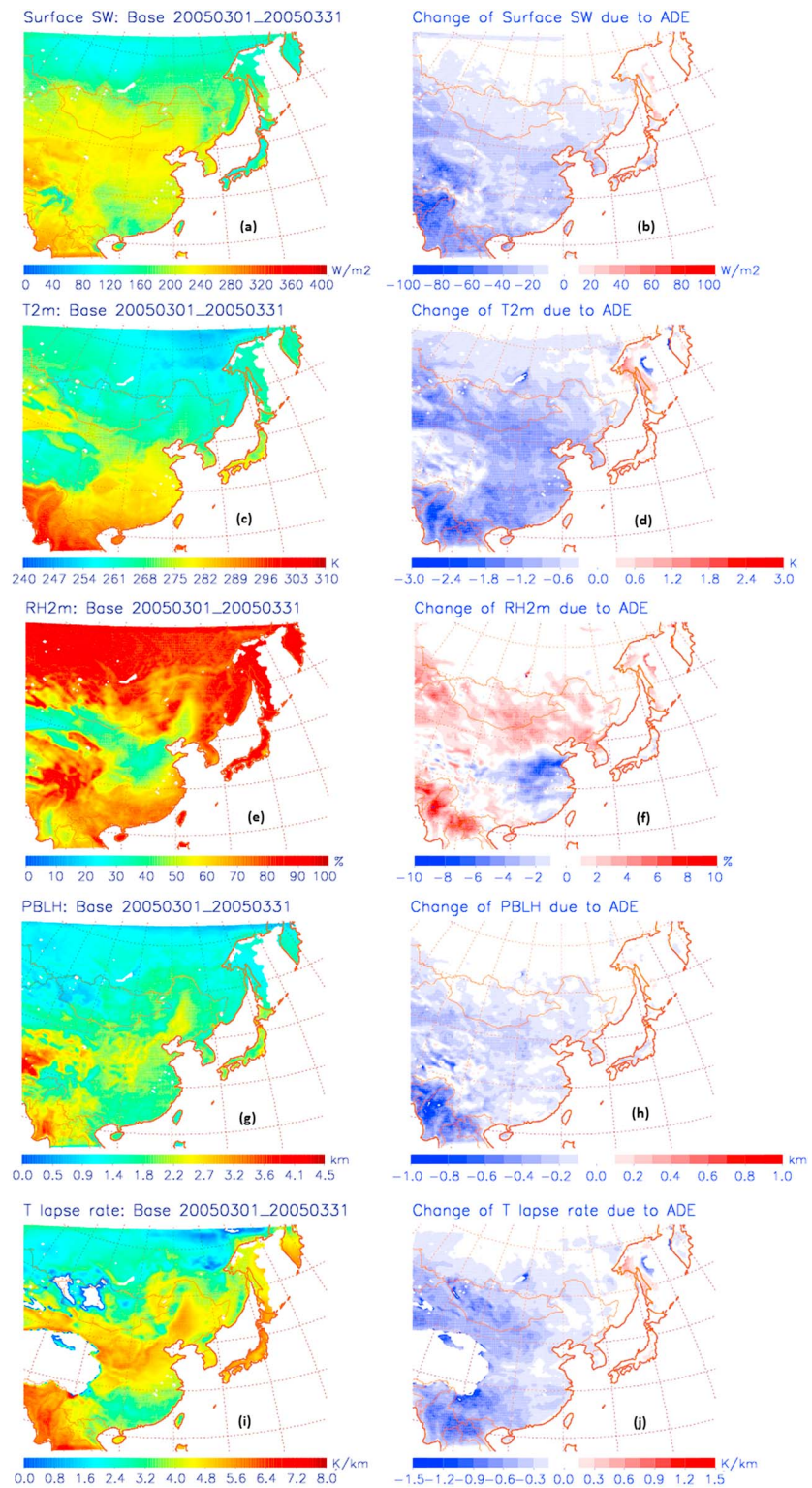


**Figure 9.** March 2005 monthly mean of hourly: (a) surface shortwave radiation, (c) temperature at 2 m, (e) relative humidity at 2 m, (g) PBLH, and (i) temperature lapse rate between 700 hPa and surface simulated by WRF-Chem Base case; (b) monthly mean of changes of surface shortwave radiation, (d) temperature at 2 m, (f) relative humidity at 2 m, (h) PBLH, and (j) temperature lapse rate between 700 hPa and surface due to the ADE.

**Table 5.** Percentage Changes of Meteorological Variables Due To ADE in Different Regions  
(Change = Base – Base\_No\_ADE)

	SWDOWN (W/m <sup>2</sup> )	T <sub>2m</sub> (K)	RH <sub>2m</sub> (%)	PBLH (m)	T Lapse Rate (K/km) <sup>a</sup>
<i>Eastern China</i>					
Mean (Base)	219.7	276.6	44.9	1262.2	4.87
Mean (Base_No_ADE)	246.9	277.7	48.2	1337.4	5.09
Change	-27.2	-1.1	-3.3	-75.2	-0.22
<i>Southern China</i>					
Mean (Base)	193.6	282.6	66.4	1206.6	3.56
Mean (Base_No_ADE)	216.4	283.7	68.1	1301.0	3.86
Change	-22.8	-1.1	-1.7	-94.4	-0.30
<i>Western China</i>					
Mean (Base)	221.5	275.3	40.4	994.4	4.47
Mean (Base_No_ADE)	252.4	276.5	38.6	1132.8	5.10
Change	-30.9	-1.2	1.8	-138.4	-0.63
<i>Sichuan Basin</i>					
Mean (Base)	194.6	281.6	58.2	1155.4	4.11
Mean (Base_No_ADE)	220.4	282.8	58.7	1266.7	4.61
Change	-27.8	-1.2	-0.5	-111.3	-0.50

<sup>a</sup>The calculation of temperature lapse rate has excluded the locations with surface pressure lower than 700 hPa.

The emissions of BC and OC are held constant; however, the dust emission will change due to ADE-related changes in soil moisture and wind speed. Figure 12 shows the distribution of dust emissions and the change due to the ADE. The dust emissions in our work are calculated by the GOCART dust scheme, using erosion and porosity data from WRF geographical input files, dust sizes, dust densities, and dust effective radius from look-up tables included in WRF-Chem, and prognostic variables from the model simulation (soil moisture and wind speed at 10 m). The maximum reduction of dust emission due to the ADE is about 8.6 kg/s per gridbox, which is about 16% of the total emission at that location (Figure 12b). Both changes of soil moisture (up to 8.6% more moist) and wind speed (up to 10% weaker wind) due to ADE contribute to the reduction of dust emission (Figures 12c and 12d), with the change of wind speed having dominant impact. However, the reduction of the dust emission does not lead to a decrease in dust aerosol concentration in most parts of western China, which implies that the change of meteorological conditions (PBLH and temperature lapse rate) are the driving factors for the change of dust aerosol due to the ADE.

The effect of the ADE on secondary aerosols, i.e., sulfate and nitrate, is different from that on primary aerosols, since the driving factors for these species differ. Under the same meteorological conditions, sulfate decreases in all four regions due to the ADE, mainly caused by the inhibited aqueous phase and gas phase reactions of SO<sub>2</sub> to form sulfate. Aqueous phase reactions between SO<sub>2</sub> and H<sub>2</sub>O<sub>2</sub> or SO<sub>2</sub> and O<sub>3</sub> are the major pathways for sulfate formation although gas phase reaction of SO<sub>2</sub> with OH is also important [Eriksen, 1972; Tanaka et al., 1994; Harris et al., 2012]. Analyses based on the difference between the Base run and the Base\_No\_ADE run show domain-wide decreases of H<sub>2</sub>O<sub>2</sub> with a maximum reduction over the Sichuan Basin (6.9%) and domain-wide decreases of ozone with a maximum reduction over Eastern China (12%) due to the ADE. Cloud water amount also decreases but only by a small amount due to the ADE. The reductions in H<sub>2</sub>O<sub>2</sub>, O<sub>3</sub>, and cloud water slow down the sulfate formation from aqueous phase reactions, thus also leading to decreased sulfate aerosols due to the ADE. The domain-wide average surface OH concentration is 0.02 parts per trillion by volume (pptv), and it is reduced by 20% because the ADE decreases the incoming solar radiation, thus slowing the photolysis of H<sub>2</sub>O<sub>2</sub> and O<sub>3</sub> to form OH. The Sichuan Basin has the highest OH concentration of the four regions, approximately 0.4 pptv in the Base\_No\_ADE run, and the percentage change of OH in Sichuan Basin is also highest (-40%). Therefore, the relatively large decrease of sulfate aerosol in Sichuan Basin is likely due to the high percentage changes in H<sub>2</sub>O<sub>2</sub> and OH there. The change of nitrate due to the ADE shows regional differences. Nitrate is enhanced in southern China, Sichuan Basin, and western China but decreased in eastern China. The composition of nitrate is mostly NH<sub>4</sub>NO<sub>3</sub>, and the formation of NH<sub>4</sub>NO<sub>3</sub> largely depends on the availability of ammonia. The surface concentration of ammonia also shows a decrease in eastern China and an increase in the other three regions (Table 6).

Ground-level ozone decreases due to the ADE. Domain-wide decreases of surface 1 h maximum ozone are shown in Figure 13, with a domain average reduction of 1.0 ppbv and a maximum decrease of 12.0 ppbv

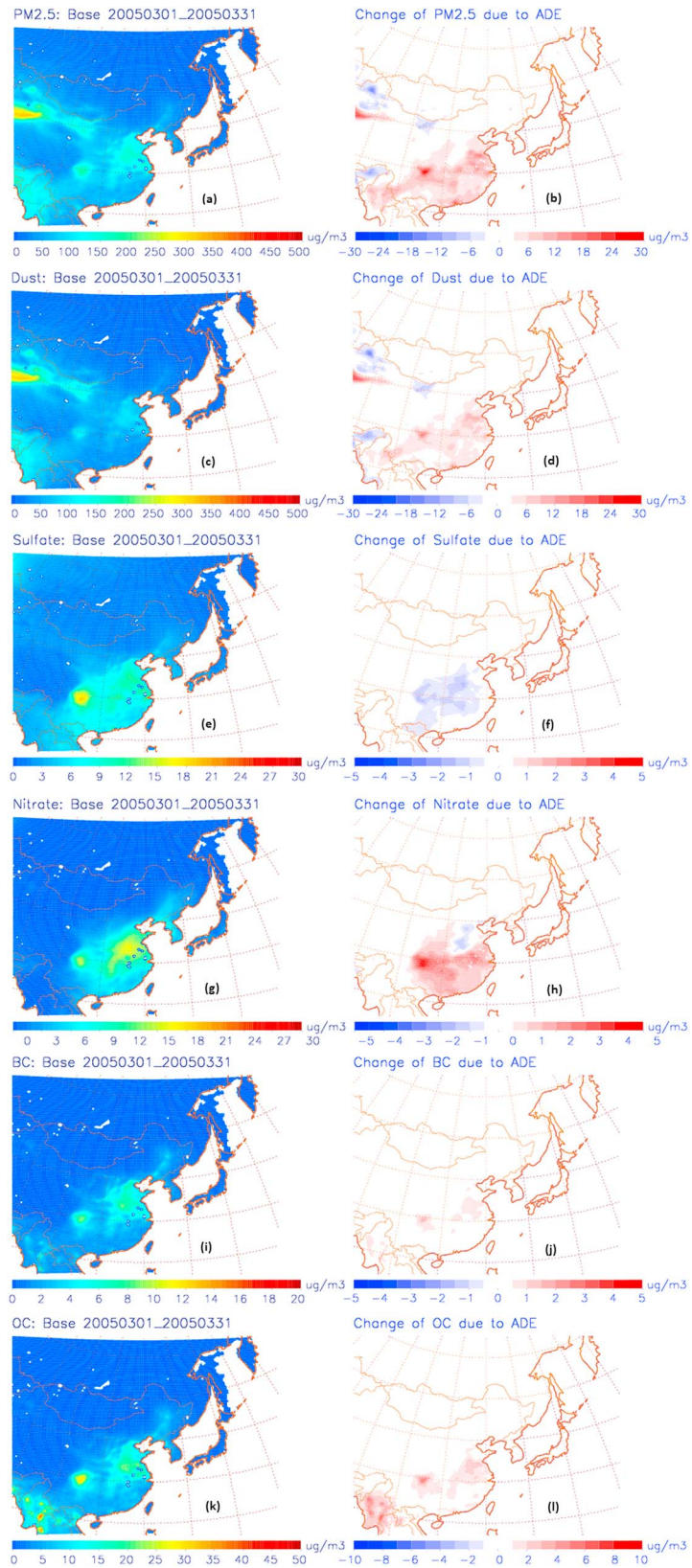


**Figure 10.** March 2005 monthly mean of surface concentration of: (a) PM<sub>2.5</sub>, (c) dust, (e) sulfate, (g) nitrate, (i) Black Carbon (BC), (k) Organic Carbon (OC) simulated by WRF-Chem Base case; monthly mean of surface concentration changes of (b) PM<sub>2.5</sub>, (d) dust, (f) sulfate, (h) nitrate, (j) Black Carbon (BC), (l) Organic Carbon (OC) due to the ADE.

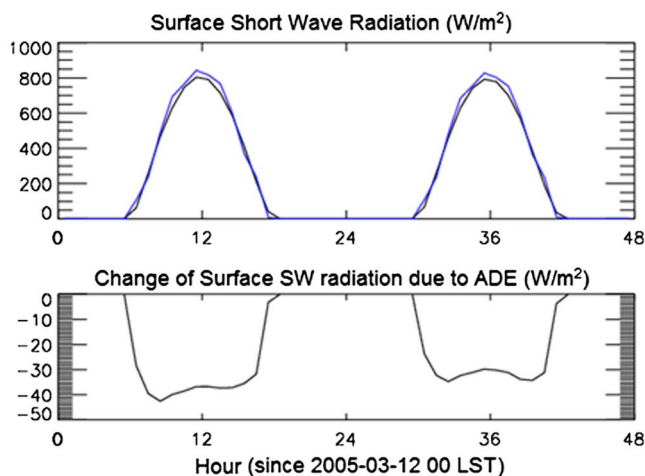


**Figure 11.** (top) Observed surface shortwave radiation at Xianghe Observatory (black) and WRF-Chem Base (blue) between 12 March 2005 00:00 and 13 March 2005 23:00 Local Standard Time (LST); (bottom) change of surface shortwave radiation due to the ADE between 12 March 2005 00:00 and 13 March 2005 23:00 LST.

located in the Sichuan Basin. Ozone is reduced because the ADE that is dominated by the effect of dust absorption leads to less solar radiation reaching the boundary layer (Figure 9b). Therefore, the photolysis process for NO<sub>2</sub> is slowed down, which leads to less tropospheric ozone formation. Meanwhile, the ADE leads to the decrease of biogenic VOC emissions, most significantly in southern China. For example, the biogenic isoprene emissions are reduced by 51% in southern China due to the ADE. The reduction in VOC emissions is partly responsible for the decrease of the surface ozone; however, it is unlikely to be the dominant factor in this season in most parts of China. The ozone dry deposition velocity also decreases due to the ADE. The dry deposition velocity is calculated based on aerodynamic resistance, quasi-laminar resistance, and surface resistance, among which the surface resistance is dominant. The surface resistance in WRF-Chem v3.3 is parameterized as a function of solar radiation, surface air temperature, surface type, and vegetation type with the Wesely scheme [Wesely, 1989]. In general, the ozone deposition velocity decreases with less surface solar radiation and cooler surface temperatures due to the ADE, with a domain average decrease of 8%. The slower photochemistry and less VOC emissions due to the ADE contribute to the decrease of surface ozone while the smaller dry deposition velocity leads to the accumulation of ozone in lower troposphere, leading to negative feedbacks between the ADE and surface ozone concentrations.

**Table 6.** Percentage Changes of PM<sub>2.5</sub> Due To ADE in Different Regions

	(Change = Base – Base_No_ADE)						
	PM <sub>2.5</sub>	Dust	Sulfate	Nitrate (μg/m <sup>3</sup> )	BC	OC	Ammonia
<i>Eastern China</i>							
Mean (Base)	116.1	71.5	8.3	10.9	5.2	13.2	6.3
Mean (Base_No_ADE)	111.2	67.3	8.9	11.0	4.8	12.2	6.5
Change	4.9 (4.4%)	4.2 (6.2%)	-0.6 (-6.7%)	-0.1 (-0.9%)	0.4 (8.3%)	1.0 (8.2%)	-0.2 (-3.1%)
<i>Southern China</i>							
Mean (Base)	75.7	44.0	7.6	8.2	2.5	7.4	5.0
Mean (Base_No_ADE)	68.9	39.9	8.0	6.6	2.2	6.5	4.7
Change	6.8 (10%)	4.1 (10.3%)	-0.4 (-5%)	1.6 (24.3%)	0.3 (13.6%)	0.9 (13.8%)	0.3 (6.4%)
<i>Western China</i>							
Mean (Base)	155.2	151.2	2.2	0.23	0.19	0.55	0.80
Mean (Base_No_ADE)	151.6	147.8	2.2	0.25	0.18	0.52	0.78
Change	3.6 (2.3%)	3.4 (2.3%)	0 (0)	0.06 (31.6%)	0.01 (5.6%)	0.03 (5.8%)	0.02 (2.6%)
<i>Sichuan Basin</i>							
Mean (Base)	115.9	68.0	12.3	8.9	4.4	14.8	7.2
Mean (Base_No_ADE)	105.7	62.1	13.3	6.4	3.9	12.9	6.7
Change	10.2 (9.6%)	5.9 (9.5%)	-1.0 (-7.5%)	2.5 (39%)	0.5 (12.8%)	1.9 (14.7%)	0.5 (7.5%)

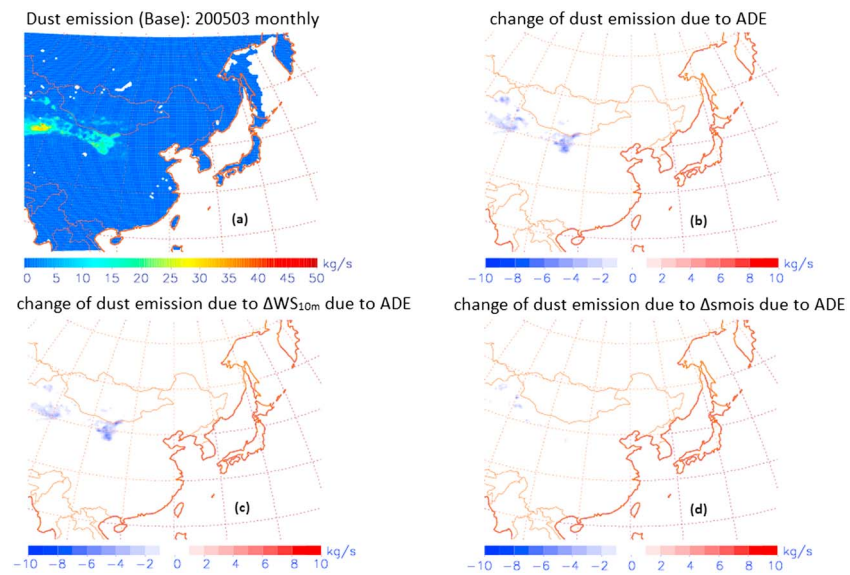


**Figure 12.** March 2005 monthly mean of dust emission: (a) surface distribution simulated by WRF-Chem Base case based on GOCART dust scheme, (b) change due to ADE, (c) change due to  $\Delta$ soil moisture caused by ADE, and (d) change due to  $\Delta$ wind speed at 10 m altitude caused by ADE.

*Forkel et al.* [2012] found increases in monthly average surface ozone in July over Germany, Eastern Europe, and southwestern France, associated with increases in surface SW radiation. They attributed most of the changes to the aerosol semidirect effect. They found that the changes in surface radiation were not correlated with aerosol amounts and inferred that they were mostly due to the cloud cover change from the semidirect effect. *Makar et al.* [2014] also studied the relative importance of aerosol direct and indirect effects on meteorology. Focusing on Europe and North America, they found that the indirect effect on meteorological fields is usually larger than the direct effect and sometimes opposes the direct effect.

We find a negative temporal correlation between aerosol loading (represented by AOD) and surface SW radiation with correlation coefficients at six WRDC stations ranging from  $-0.50$  to  $-0.82$  (Figure 8), suggesting that the aerosol loading is an important factor determining the temporal variation of the surface SW radiation. However, the semidirect effect also plays a role as the cloud optical depth (CODs) decreases over much of the domain. This decrease in COD increases surface SW radiation and ambient ozone and partially counters the increase in SW radiation and ozone due to the ADE. The large aerosol loading and relatively low water vapor concentrations in our domain during this season may cause the stronger ADE and weaker semidirect effect in our case compared to *Forkel et al.* [2012].

### 3.3. Impact of Future Emission Reductions

SO<sub>2</sub> emissions declined 15% between 2005 and 2010 due to large-scale deployment of flue gas desulfurization (FGD) at China's power plants [C. Li *et al.*, 2010; S. X. Wang *et al.*, 2014]. Assuming best available technologies are fully implemented, SO<sub>2</sub> emissions in 2030 should be reduced to 27% of the 2010 level [S. X. Wang *et al.*, 2014]. The RCP4.5 emission scenario estimates 2050 SO<sub>2</sub> emission to be 20% of that in 2005. Therefore, we assume that the SO<sub>2</sub> emissions will decrease by 80% in 2050 compared to the 2005 level and apply this reduction in our sensitivity run (SO<sub>2</sub> × 0.2\_ADE). With less SO<sub>2</sub> emission, surface shortwave radiation increases, especially south of 30°N. Surface temperatures are higher with emission reductions with the maximum increase about 0.15 K in China. By emitting less SO<sub>2</sub>, the air quality is mostly improved (Figure 14). SO<sub>2</sub> is the precursor of sulfate aerosol, a scattering aerosol. Regulating SO<sub>2</sub> leads to changes of the scattering aerosols. The impact on PM<sub>2.5</sub> concentration is most significant over the Sichuan basin and southern China, with reductions of up to 17.5 μg/m<sup>3</sup> in Sichuan Basin and southern China and a regional average decrease of 5.4%. However, in this simulation reducing SO<sub>2</sub> emissions leads to an increase of PM<sub>2.5</sub> over dusty areas in western China as dust emissions increase due to ADE-induced changes that are shown in Figure 12. The surface 1 h maximum ozone concentration goes down by up to 6 ppbv in Sichuan Basin and up to 4 ppbv

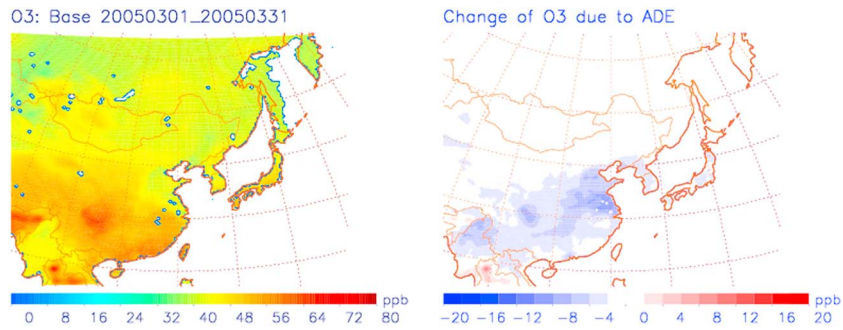


**Figure 13.** March 2005 monthly mean of surface 1 h maximum ozone: (left) surface distribution simulated by WRF-Chem Base case; (right) change due to ADE.

in eastern China. This result is consistent with the study by *Dickerson et al.* [1997] indicating that the scattering aerosol accelerates boundary layer ozone production since scattering of UV radiation enhances the actinic flux and simultaneously the photolysis rate in the boundary layer. Therefore, in our sensitivity run, reducing  $\text{SO}_2$  emissions is also beneficial for reducing ozone pollution.

The total BC emission in China from INTEX-B emission inventory was 1811 Gg/yr, while the total black carbon emission from U.S. was 580 Gg in 2005 (Report to Congress on Black Carbon, [EPA, 2012]) and continued to decrease. Assuming the best control technologies are available and the rigorous regulations are fully implemented, the BC emission in China is expected to decrease to the current U.S. level by 2050, approximately 20% of the INTEX-B level. The sensitivity simulation ( $\text{BC} \times 0.2$ ) tested the impact of reducing BC emissions to 20% of INTEX-B levels. BC is mainly a primary aerosol; i.e., it is emitted directly. The surface radiation and surface temperature are both enhanced due to BC emission reductions, similar to the case with less  $\text{SO}_2$  emission. The  $\text{PM}_{2.5}$  level declines, especially in the Sichuan Basin (up to  $13 \mu\text{g}/\text{m}^3$ ) and eastern China (up to  $6.8 \mu\text{g}/\text{m}^3$ ). However, the ozone pollution worsens in the Sichuan Basin (increases of up to 3.2 ppbv) and parts of eastern China (increases of up to 3.6 ppbv) (Figure 14). Reducing absorbing aerosols allows more short-wave radiation to reach the surface, therefore increases the photolysis rate, and accelerates the photochemistry of ozone production.

#### 4. Conclusion

WRF-Chem sensitivity simulations were conducted in East Asia for the EAST-AIRE IOC period (March 2005) to investigate the ADE on surface radiation and air quality. Comparison between model and in situ and satellite

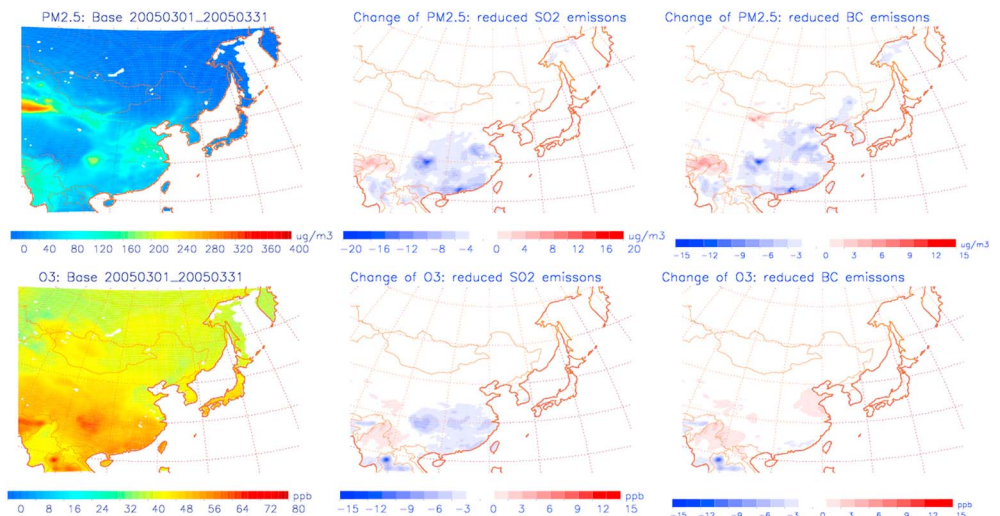


**Figure 14.** Change of surface  $\text{PM}_{2.5}$  concentration and surface ozone concentration due to  $\text{SO}_2$  and BC emission reductions.

observations demonstrated that WRF-Chem when run with the configuration shown in Table 1 captured the temporal and spatial variations of meteorological fields, trace gases, and aerosol loadings reasonably well. However, WRF-Chem underestimated some peak values of trace gases (CO, SO<sub>2</sub>) and AOD, partly due to the biases in simulated wind fields and the coarse resolution of emission inventories. Scattering by aerosols was underestimated in the model, leading to the AOD underestimation.

We found that the effect of ADE on surface SW radiation is  $-20 \text{ W/m}^2$  domain wide, with a value of  $-25 \text{ W/m}^2$  at Xianghe Observatory, consistent with observations. The ADE caused diverse changes in PM<sub>2.5</sub> and its components in four regions of China with high PM<sub>2.5</sub> loading. The surface PM<sub>2.5</sub> level was enhanced domain wide due to ADE, with 4.4% in eastern China, 10% in southern China, 2.3% in western China, and 9.6% in the Sichuan Basin. The concentrations of primary aerosols (dust, BC, and OC) increase in the four regions mainly driven by the thinner PBLH and higher atmospheric stability caused by the ADE. The changes of secondary aerosols (sulfate and nitrate) due to the ADE show different signals compared to primary aerosols, largely driven by the change of the chemistry such as the oxidation capacity of the atmosphere. The ADE leads to domain-wide decrease in sulfate, with the maximum in Sichuan Basin ( $-7.5\%$ ). Nitrate increases in southern China, western China, and the Sichuan Basin but decreases in eastern China, consistent with the change of ammonia aerosol.

Two sensitivity simulations were carried out to test the potential impact of emission reductions on East Asian air quality. Our study with reduced BC and SO<sub>2</sub> emissions indicates that reducing absorbing aerosols could lead to an increase in certain gas pollutants (i.e., ozone) if emissions of NO<sub>x</sub> and VOC are unchanged, while reducing scattering aerosols would have cobenefits in ozone pollution. Thus, policy makers need to take the aerosol types and the interaction between aerosols and other air pollutants into account when implementing PM regulations.

## Appendix A

The photolysis rate of trace gas  $j$  ( $J$  value) is calculated by

$$J(i) = \int_{\lambda_1}^{\lambda_2} \sigma_i(\lambda, T) \phi_i(\lambda, T) F(\lambda) d\lambda, \quad (\text{A1})$$

where  $\sigma_i(\lambda, T)$  (in the unit of  $\text{cm}^2$ ) is the wavelength and temperature-dependent absorption cross section of species  $i$ ,  $\phi_i(\lambda, T)$  is the quantum yield, and  $F(\lambda)$  (in the unit of  $\text{photons cm}^{-2} \text{ nm}^{-1} \text{ s}^{-1}$ ) is the solar actinic flux. In our work, the FAST-J photolysis algorithm [Wild *et al.*, 2000] is applied to compute the actinic flux. Determination of actinic flux at each vertical layer depends on the attenuation of incoming solar radiation; therefore, optical properties for scattering and absorption by molecules, aerosols, and cloud droplets throughout the vertical extent need to be specified. In FAST-J, these optical properties are expressed as the optical thickness,  $\tau$ ; the single-scattering albedo,  $\omega_0$ ; and the scattering phase function,  $p(\theta)$  as a function of wavelength  $\lambda$ . The optical thickness ( $\tau$ ) is the sum of molecular (Rayleigh) scattering, gaseous absorption by ozone, aerosol extinction, and cloud optical thickness. Rayleigh scattering is solely dependent on the pressure, therefore easily determined. Absorption by ozone is given by the prognostic ozone profile from WRF-Chem. Cloud optical depths are treated by using fractional cloudiness based on relative humidity in the photolysis module in WRF-Chem. The default version of WRF-Chem uses a lookup table with prescribed aerosol optical properties to calculate the actinic flux; therefore, the model aerosols have no impact on the photolysis rates. We have implemented a link between prognostic aerosol concentrations and the Fast-J module. The aerosol mass concentration in eight bins is passed to a subroutine inside module\_optical\_averaging.F to calculate aerosol number density in each bin, effective radius, and refractive index. Then this information is used in a module (mieaer) based on Mie theory to calculate the prognostic aerosol size distribution, extinction coefficient, single-scattering albedo, asymmetry parameter, and aerosol optical depth, which are applied in the calculation of actinic flux in Fast-J module.

In order to test our implementation of the aerosol photolysis link, we performed 1 day sensitivity simulations to test the impact of the prognostic sulfate and black carbon on the photolysis rate in WRF-Chem assuming cloud-free conditions. We selected one simulation day (15 March 2005) and performed three sensitivity simulations: (1) no aerosol in Fast-J module, (2) only sulfate in Fast-J module, and (3) only black carbon in Fast-J module. We examined the impact of sulfate and black carbon on the NO<sub>2</sub> photolysis rate at Xianghe station at 12 UTC. The total burden of sulfate and black carbon is assumed to be  $110 \text{ mg/m}^2$  and  $25 \text{ mg/m}^2$ . About

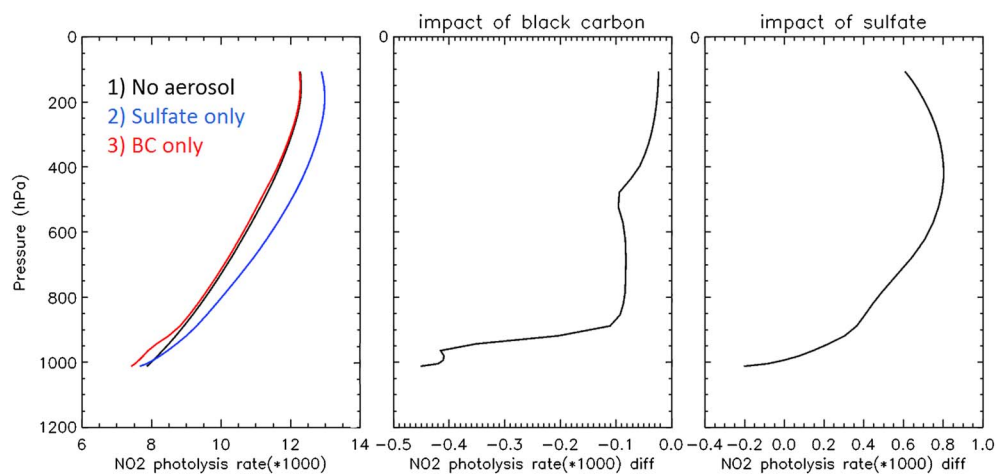


**Figure A1.** (left)  $\text{NO}_2$  photolysis rate ( $\text{s}^{-1}$ ) from three simulations: No aerosol in Fast-J module (black), sulfate only (blue), and BC only (red). (middle) Impact of black carbon on  $\text{NO}_2$  photolysis rate ( $\text{s}^{-1}$ ). (right) Impact of sulfate on  $\text{NO}_2$  photolysis rate ( $\text{s}^{-1}$ ).

90% of black carbon is concentrated below 300 m, decreasing rapidly with height. Sulfate is abundant near surface and around 500 m due to  $\text{SO}_2$  emissions from both industrial/residential sources at surface and power plant emissions aloft. The absorbing aerosol black carbon reduces the  $\text{NO}_2$  photolysis rate at all the vertical layers with the largest reduction near the surface (Figure A1, left and middle). On the other hand, the scattering aerosol sulfate decreases the  $\text{NO}_2$  photolysis rate near surface but increases it at higher layers (Figure A1, left and right), because sulfate is mostly backscattering, blocking the radiation below the sulfate aerosol layer, but enhancing the radiation at upper levels by scattering the radiation back.

The results are consistent with a previous study by Liao *et al.* [1999]. They used the one-dimensional discrete ordinate radiative transfer model [Stamnes *et al.*, 1988] to investigate the effects of  $(\text{NH}_4)_2\text{SO}_4$  and soot on the  $j(\text{O}_3 \rightarrow \text{O}^1\text{D})$ ,  $j(\text{NO}_2)$ , and  $j(\text{HCHO})$  profile under clear-sky and cloudy-sky conditions. They assumed column burdens of  $125 \text{ mg m}^{-2}$  for  $(\text{NH}_4)_2\text{SO}_4$  and  $25 \text{ mg m}^{-2}$  for soot under polluted urban conditions, with the mass concentration of each species decreasing linearly from its value at the surface to 0.1 of its surface value at 3 km altitude and remaining constant from 3 to 5 km. They also found that in the clear-sky condition, soot aerosol reduces photolysis rates at all altitudes, whereas sulfate aerosol generally increases photolysis rates above and in the upper part of the aerosol layer but reduces photolysis rates in the lower part of the aerosol layer and at the surface [Liao *et al.*, 1999, Figures 3 and 4].

#### Acknowledgments

This research was sponsored by a NASA Interdisciplinary Science Investigation through NASA grants NNX08AR42G and NNX12AH79G, MOST (2013CB955804), and NSFC (91544217). We acknowledge the free use of tropospheric  $\text{NO}_2$  and HCHO column data from the OMI sensor from www.temis.nl. We also gratefully thank AeroStat Giovanni team (<http://giovanni.gsfc.nasa.gov/aerostat/>) for providing MODIS data collocated with AERONET sites. The surface radiation data are kindly provided by WRDC (<http://wrdc.mgo.rssi.ru/>) that is sponsored by WMO. The EAST-AIRE campaign data are maintained and provided by Maureen Cribb of ESSIC/University of Maryland, College Park.

#### References

- Barnard, J. C., E. G. Chapman, J. D. Fast, J. R. Schmelzer, J. R. Schlusser, and R. E. Shetter (2004), An evaluation of the FAST-J photolysis model for predicting nitrogen dioxide photolysis rates under clear and cloudy sky conditions, *Atmos. Environ.*, **38**, 3393–3403.
- Boersma, K. F., et al. (2011), An improved tropospheric  $\text{NO}_2$  column retrieval algorithm for the Ozone Monitoring Instrument, *Atmos. Meas. Tech.*, **4**, 1905–1928.
- Chen, F., and J. Dudhia (2001), Coupling an advanced land-surface/hydrology model with the Penn State/NCAR MM5 modeling system. Part I: Model description and implementation, *Mon. Weather Rev.*, **129**, 569–585.
- Chou, M.-D., and M. J. Suarez (1994), *An Efficient Thermal Infrared Radiation Parameterization for Use in General Circulation Models*, NASA Tech. Memo. 104606, vol. 3, 85 pp, NASA, Greenbelt, Md.
- Dickerson, R. R., S. Kondragunta, G. Stenchikov, K. L. Civerolo, B. G. Doddridge, and B. N. Holben (1997), The impact of aerosols on solar ultraviolet radiation and photochemical smog, *Science*, **278**(5339), 827–830, doi:10.1126/science.278.5339.827.
- Dockery, D. W., C. A. Pope, X. Xu, J. D. Spengler, J. H. Ware, M. E. Fay, B. G. Ferris Jr., and F. E. Speizer (1993), An association between air pollution and mortality in six U.S. cities, *N. Engl. J. Med.*, **329**, 1753–1759.
- Emmons, L. K., et al. (2010), Description and evaluation of the model for ozone and related chemical tracers, version 4 (MOZART-4), *Geosci. Model Dev.*, **3**, 43–67, doi:10.5194/gmd-3-43-2010.
- EPA (2012), Report Congress on Black Carbon, 388 pp., U.S. Environmental Protection Agency, Washington, D. C.
- Eriksen, T. E. (1972), Sulfur isotope effects: 1. Isotopic exchange coefficient for sulfur isotopes  $34\text{S}$ – $32\text{S}$  in system  $\text{SO}_2(\text{g})$ – $\text{HSO}_3(\text{aq})$  at 25, 35, and 45 degrees C, *Acta Chem. Scand.*, **26**, 573.
- Fast, J. D., W. I. Gustafson Jr., R. C. Easter, R. A. Zaveri, J. C. Barnard, E. G. Chapman, G. A. Grell, and S. E. Peckham (2006), Evolution of ozone, particulates, and aerosol direct radiative forcing in the vicinity of Houston using a fully coupled meteorology-chemistry-aerosol model, *J. Geophys. Res.*, **111**, D21305, doi:10.1029/2005JD006721.
- Forkel, R., J. Werhahn, A. B. Hansen, S. McKeen, S. Peckham, G. Grell, and P. Suppan (2012), Effect of aerosol-radiation feedback on regional air quality: A case study with WRF/Chem, *Atmos. Environ.*, **53**, 202–211.

- Fuglestedt, J. S., J. E. Jonson, and I. S. A. Isaksen (1994), Effects of reductions in stratospheric ozone on tropospheric chemistry through changes in photolysis rates, *Tellus, Ser. B*, *46*, 172–192.
- Ghan, S. J. (2013), Technical note: Estimating aerosol effects on cloud radiative forcing, *Atmos. Chem. Phys.*, *13*, 9971–9974, doi:10.5194/acp-13-9971-2013.
- Grell, G. A., and D. Devenyi (2002), A generalized approach to parameterizing convection combining ensemble and data assimilation techniques, *Geophys. Res. Lett.*, *29*(14), 1693, doi:10.1029/2002GL015311.
- Grell, G. A., S. E. Peckham, R. Schmitz, S. A. McKeen, G. Frost, W. C. Skamarock, and B. Eder (2005), Fully coupled “online” chemistry within the WRF model, *Atmos. Environ.*, *39*, 6957–6975.
- Guenther, A., et al. (1995), Global-model of natural volatile organic-compound emissions, *J. Geophys. Res.*, *100*, 8873–8892, doi:10.1029/94JD02950.
- Guenther, A., T. Karl, P. Harley, C. Wiedinmyer, P. I. Palmer, and C. Geron (2006), Estimates of global terrestrial isoprene emissions using MEGAN (Model of Emissions of Gasses and Aerosols from Nature), *Atmos. Chem. Phys.*, *6*, 3181–3210.
- Harris, E., B. Sinha, P. Hoppe, J. N. Crowley, S. Ono, and S. Foley (2012), Sulfur isotope fractionation during oxidation of sulfur dioxide: Gas-phase oxidation by OH radicals and aqueous oxidation by H<sub>2</sub>O<sub>2</sub>, O<sub>3</sub> and iron catalysis, *Atmos. Chem. Phys.*, *12*, 407–424.
- Harrison, R. M., and J. Yin (2000), Particulate matter in the atmosphere: Which particle properties are important for its effects on health?, *Sci. Total Environ.*, *249*(1–3), 85–101.
- Holben, B. N., et al. (1998), AERONET—A federated instrument network and data archive for aerosol characterization, *Remote Sens. Environ.*, *66*, 1–16, doi:10.1016/S0034-4257(98)00031-5.
- Hong, S., Y. Noh, and J. Dudhia (2006), A new vertical diffusion package with an explicit treatment of entrainment processes, *Mon. Weather Rev.*, *134*, 2318–2341.
- Hsu, N. C., R. Gautam, A. M. Sayer, C. Bettenhausen, C. Li, M. J. Jeong, S.-C. Tsay, and B. N. Holben (2012), Global and regional trends of aerosol optical depth over land and ocean using SeaWiFS measurements from 1997 to 2010, *Atmos. Chem. Phys.*, *12*, 8037–8053.
- Huang, K., G. Zhang, Q. Wang, J. S. Fu, Y. Lin, T. Liu, L. Han, and C. Deng (2014), Extreme haze pollution in Beijing during January 2013: Chemical characteristics, formation mechanism and role of for processing, *Atmos. Chem. Phys. Discuss.*, *14*, 7517–7556.
- Huang, R.-J., et al. (2014), High secondary aerosol contribution to particulate pollution during haze events in China, *Nature*, *514*, 218–222.
- Huang, X., Y. Song, M. Li, J. Li, Q. Huo, X. Cai, T. Zhu, M. Hu, and H. Zhang (2012), A high-resolution ammonia emission inventory in China, *Global Biogeochem. Cycles*, *26*, GB1030, doi:10.1029/2011GB004161.
- Intergovernmental Panel on Climate Change (2014), *Climate Change 2014: Synthesis Report. Contribution of Working Groups I, II and III to the Fifth Assessment Report of the Intergovernmental Panel on Climate Change*, edited by Core Writing Team, R. K. Pachauri, and L. A. Meyer, 151 pp., IPCC, Geneva, Switzerland.
- Jiang, F., Q. Liu, X. Huang, T. Wang, B. Zhuang, and M. Xie (2012), Regional modeling of secondary organic aerosol over China using WRF/Chem, *J. Aerosol Sci.*, *43*(1), 57–73.
- Levelt, P. F., G. H. J. van den Oord, M. R. Dobber, A. Malkki, H. Visser, J. de Vries, P. Stammes, J. O. V. Lundell, and H. Saari (2006), The Ozone Monitoring Instrument, *IEEE Trans. Geosci. Remote Sens.*, *44*, 1093–1101, doi:10.1109/TGRS.2006.872333.
- Li, C., L. T. Marufu, R. R. Dickerson, Z. Li, T. Wen, Y. Wang, P. Wang, H. Chen, and J. W. Stehr (2007), In situ measurements of trace gases and aerosol optical properties at a rural site in northern China during East Asian Study of Tropospheric Aerosols: An International Regional Experiment 2005, *J. Geophys. Res.*, *112*, D22S04, doi:10.1029/2006JD007592.
- Li, C., Q. Zhang, N. A. Krotkov, D. G. Street, K. He, S. Tsay, and J. F. Gleason (2010), Recent large reduction in sulfur dioxide emissions from Chinese power plants observed by the Ozone Monitoring Instrument, *Geophys. Res. Lett.*, *37*, L08807, doi:10.1029/2010GL042594.
- Li, Z., and Z. Yan (2009), Homogenized daily mean/maximum/minimum temperature series for China from 1960–2008, *Atmos. Oceanic Sci. Lett.*, *2*(4), 237–243.
- Li, Z., et al. (2007), Preface to special section on East Asian Studies of Tropospheric Aerosols: An International Regional Experiment (EASTAIRE), *J. Geophys. Res.*, *112*, D22S00, doi:10.1029/2007JD008853.
- Li, Z., K.-H. Lee, J. Xin, Y. Wang, and W.-M. Hao (2010), First observation-based estimates of cloud-free aerosol radiative forcing across China, *J. Geophys. Res.*, *115*, D00K18, doi:10.1029/2009JD013306.
- Li, Z., et al. (2011), East Asian Studies of Tropospheric Aerosols and their Impact on Regional Climate (EASTAIRC): An overview, *J. Geophys. Res.*, *116*, D00K34, doi:10.1029/2010JD015257.
- Liao, H., Y. L. Yung, and J. H. Seinfeld (1999), Effects of aerosol on tropospheric photolysis rates in clear and cloudy atmospheres, *J. Geophys. Res.*, *104*, 23,697–23,707, doi:10.1029/1999JD900409.
- Liu, S. C., and M. Trainer (1988), Responses of the tropospheric ozone and odd hydrogen radicals to column ozone change, *J. Atmos. Chem.*, *6*, 221–233.
- Ma, J. (1995), Effects of stratospheric ozone depletion on tropospheric chemistry through changes in UV-B radiation, TNO-MW-R-95/127, Neth. Organ. for Appl. Sci., Delft, Netherland.
- Madronich, S., and C. Granier (1992), Impact of recent total ozone changes on tropospheric ozone photodissociation, hydroxyl radicals, and methane trends, *Geophys. Res. Lett.*, *19*, 465–467, doi:10.1029/92GL00378.
- Makar, P., W. Gong, J. Milbrandt, C. Hogrefe, Y. Zhang, G. Curci, R. Zabkar, U. Im, A. Balzarini, and R. Baró (2014), Feedbacks between air pollution and weather. Part 1: Effects on weather, *Atmos. Environ.*, *115*, 442–469.
- Mlawer, E. J., S. J. Taubman, P. D. Brown, M. J. Iacono, and S. A. Cloug (1997), RRTM, a validated correlated-k model for the longwave, *J. Geophys. Res.*, *102*, 16,663–16,682, doi:10.1029/97JD00237.
- Morrison, H., G. Thompson, and V. Tatarskii (2009), Impact of cloud microphysics on the development of trailing stratiform precipitation in a simulated squall line: Comparison of one- and two-moment schemes, *Mon. Weather Rev.*, *137*, 991–1007, doi:10.1175/2008mwr2556.1.
- Mu, M., et al. (2010), Daily and 3-hourly variability in global fire emissions and consequences for atmospheric model predictions of carbon monoxide, *J. Geophys. Res.*, *116*, D24303, doi:10.1029/2011JD016245.
- Remer, L. A., et al. (2005), The MODIS aerosol algorithm, products, and validation, *J. Atmos. Sci.*, *62*, 947–973, doi:10.1175/JAS3385.1.
- Remer, L. A., et al. (2008), Global aerosol climatology from MODIS satellite sensors, *J. Geophys. Res.*, *113*, D14S07, doi:10.1029/2007JD009661.
- Seinfeld, J. H., and S. N. Pandis (2006), *Atmospheric Chemistry and Physics: From Air Pollution to Climate Change*, John Wiley, New York.
- Singh, H. B., W. H. Brune, J. H. Crawford, F. Flocke, and D. J. Jacob (2009), Chemistry and transport of pollution over the Gulf of Mexico and the Pacific: Spring 2006 INTEX-B campaign overview and first results, *Atmos. Chem. Phys.*, *9*, 2301–2318, doi:10.5194/acp-9-2301-2009.
- Stammes, K., S. C. Tsay, W. Wiscombe, and K. Jayaweera (1988), Numerically stable algorithm for discrete-ordinate-method radiative transfer in multiple scattering and emitting layered media, *Appl. Opt.*, *27*(12), 2502–2509.
- Storer, R. L., S. C. van den Heever, and T. S. L'Ecuyer (2014), Observations of aerosol-induced convective invigoration in the tropical east Atlantic, *J. Geophys. Res. Atmos.*, *119*, 3963–3975, doi:10.1002/2013JD020272.

- Sukoriansky, S., B. Galperin, and V. Perov (2005), Application of a new spectral model of stratified turbulence to the atmospheric boundary layer over sea ice, *Boundary Layer Meteorol.*, *117*, 231–257.
- Tanaka, N., D. M. Rye, Y. Xiao, and A. C. Lasaga (1994), Use of stable sulfur isotope systematics for evaluating oxidation reaction pathways and in-cloud scavenging of sulfur-dioxide in the atmosphere, *Geophys. Res. Lett.*, *21*, 1519–1522, doi:10.1029/94GL00893.
- Tang, Y., et al. (2004), Impacts of dust on regional tropospheric chemistry during the ACE-Asia experiment: A model study with observations, *J. Geophys. Res.*, *109*, D19S21, doi:10.1029/2003JD003806.
- Thompson, A. M., M. A. Owens, and R. W. Stewart (1989), Sensitivity of tropospheric oxidants to global chemical and climate change, *Atmos. Environ.*, *23*, 516–532.
- Tie, X. X., S. Madronich, S. Walters, D. P. Edwards, P. Ginoux, N. Mahowald, R. Y. Zhang, C. Lou, and G. Brasseur (2005), Assessment of the global impact of aerosols on tropospheric oxidants, *J. Geophys. Res.*, *110*, D03204, doi:10.1029/2004JD005359.
- van der Werf, G. R., J. T. Randerson, L. Giglio, G. J. Collatz, M. Mu, P. S. Kasibhatla, D. C. Morton, R. S. DeFries, Y. Jin, and T. T. van Leeuwen (2010), Global fire emissions and the contribution of deforestation, savanna, forest, agricultural, and peat fires (1997–2009), *Atmos. Chem. Phys.*, *10*, 11,707–11,735, doi:10.5194/acp-10-11707-2010.
- Wang, H., G. Shi, X. Zhang, S. Gong, S. Tan, B. Chen, H. Che, and T. Li (2015), Mesoscale modelling study of the interactions between aerosols and PBL meteorology during a haze episode in China Jing-Jin-Ji and its near surrounding region—Part 2: Aerosols' radiative feedback effects, *Atmos. Chem. Phys.*, *15*, 3277–3287.
- Wang, L. T., Z. Wei, J. Yang, Y. Zhang, F. F. Zhang, J. Su, C. C. Meng, and Q. Zhang (2014), The 2013 severe haze over southern Hebei, China: Model evaluation, source apportionment, and policy implications, *Atmos. Chem. Phys.*, *14*, 3151–3173, doi:10.5194/acp-14-3151-2014.
- Wang, S. X., et al. (2014), Emission trends and mitigation options for air pollutants in East Asia, *Atmos. Chem. Phys.*, *14*, 6571–6603, doi:10.5194/acp-14-6571-2014.
- Wesely, M. L. (1989), Parameterization of surface resistances to gaseous dry deposition in regional-scale numerical models, *Atmos. Environ.*, *23*, 1293–1304.
- Wild, O., X. Zhu, and M. J. Prather (2000), Fast-J: Accurate simulation of in- and below cloud photolysis in tropospheric chemical models, *J. Atmos. Chem.*, *37*, 245–282.
- Xia, X., Z. Li, P. Wang, H. Chen, and M. Cribb (2007), Estimation of aerosol effects on surface irradiance based on measurements and radiative transfer model simulations in northern China, *J. Geophys. Res.*, *112*, D22S10, doi:10.1029/2006JD008337.
- Xin, J., et al. (2007), Aerosol optical depth (AOD) and Ångström exponent of aerosols observed by the Chinese Sun Hazemeter Network from August 2004 to September 2005, *J. Geophys. Res.*, *112*, D05203, doi:10.1029/2006JD007075.
- Zaveri, R. A., and L. K. Peters (1999), A new lumped structure photochemical mechanism for large-scale applications, *J. Geophys. Res.*, *104*, 30,387–30,415, doi:10.1029/1999JD900876.
- Zaveri, R. A., R. C. Easter, J. D. Fast, and L. K. Peters (2008), Model for Simulating Aerosol Interactions and Chemistry (MOSAIC), *J. Geophys. Res.*, *113*, D13204, doi:10.1029/2007JD008782.
- Zhang, Q., D. G. Streets, and G. R. Carmichael (2009), Asian emissions in 2006 for the NASA INTEX-B mission, *Atmos. Chem. Phys.*, *9*, 5131–5153.
- Zhao, C., and Y. Wang (2009), Assimilated inversion of NO<sub>x</sub> emissions over east Asia using OMI NO<sub>2</sub> column measurements, *Geophys. Res. Lett.*, *36*, L06805, doi:10.1029/2008GL037123.